Doping-dependent critical current properties in K, Co, and P-doped BaFe$_2$As$_2$ single crystals

Shigeyuki Ishida, Dongjoon Song, Hiraku Ogino, Akira Iyo, and Hiroshi Eisaki

Electronics and Photonics Research Institute, National Institute of Advanced Industrial Science and Technology, Tsukuba 305-8568, Japan

Masamichi Nakajima

Department of Physics, Osaka University, Toyonaka, Osaka 560-0043, Japan

Jun-ichi Shimoyama

Department of Physics and Mathematics, Aoyama Gakuin University, Sagamihara 252-5258, Japan

Michael Eisterer

Atominstitut, TU Wien, Stadionallee 2, 1020 Vienna, Austria

In order to establish the doping dependence of the critical current properties in the iron-based superconductors, the in-plane critical current density J_c of BaFe$_2$As$_2$-based superconductors Ba$_{1-x}$K$_x$Fe$_2$As$_2$ (K-Ba122), Ba(Fe$_{1-x}$Co$_x$)$_2$As$_2$ (Co-Ba122), and BaFe$_2$(As$_{1-x}$P$_x$)$_2$ (P-Ba122) in a wide range of doping concentration x was investigated by means of magnetization hysteresis loop (MHL) measurements on single-crystal samples. Depending on the dopant elements and their concentration, J_c exhibits a variety of magnetic-field H and temperature T dependences. (1) In the case of K-Ba122, the MHL of the underdoped samples ($x \leqslant 0.33$) exhibits a second magnetization peak (SMP), which sustains high J_c at high H and high T, exceeding 10^5 A/cm^2 at $T = 25$ K and $\mu_0 H = 6$ T for $x = 0.30$. On the other hand, the SMP is missing in the optimally ($x \sim 0.36$–0.40) and overdoped ($x \sim 0.50$) samples and consequently J_c rapidly decreases by more than one order of magnitude, although the change in T_c is within a few K. (2) For Co-Ba122, the SMP is always present over the entire superconducting (SC) dome from the underdoped ($x \sim 0.05$) to the overdoped ($x \sim 0.12$) region. However, the magnitude of J_c significantly changes with x, exhibiting a sharp maximum at $x \sim 0.057$, which is a slightly underdoped composition for Co-Ba122. (3) For P-Ba122, the highest J_c is attained at $x = 0.30$, corresponding to the highest T_c composition. For the overdoped samples, the MHL is characterized by a SMP located close to the irreversibility field H_{irr}. Common to the three doping variations, J_c becomes highest at the underdoping side of the SC dome near the phase boundary between the SC phase and the antiferromagnetic-orthorhombic (AFO) phase. Also, the peak appears in a narrow range of doping, distinct from the T_c dome with a broad maximum. These similarities in the three cases indicate that the observed doping dependence of J_c is intrinsic to the BaFe$_2$As$_2$-based superconductors. The scaling analysis of the normalized pinning force density f_p as a function of the reduced magnetic field $h = H/H_{irr}$ shows that the peak position in the pinning force h_{max} depends on x, indicating a change in pinning with x. On the other hand, high-J_c samples always attain similar h_{max} values of 0.40–0.45 for all the dopants, which may suggest that a common pinning source causes the highest J_c. A quantitative analysis of the T-dependent J_c indicates that the two pinning mechanisms, namely, the spatial variations in T_c (referred to as δT_c pinning) and the fluctuations in the mean free path (δl pinning), are enhanced for the underdoped samples, which results in the enhancement of J_c. Possible origins for the different pinning mechanism are discussed in connection with the x dependence of T_c, the residual resistivity, AFO domain boundaries, and a possible quantum critical point.

I. INTRODUCTION

The investigation of the critical current J_c properties is one of the main topics in the research of the Fe-based high-transition-temperature (high-T_c) superconductors. Fe-based superconductors are considered as promising candidates for large-current and/or high-magnetic-field applications, since they possess considerably high T_c, reaching 56 K at highest, as well as high upper critical magnetic fields H_{c2}, exceeding 100 T with moderate anisotropy ($\gamma = H_{c2}^{ab}/H_{c2}^c = 1$–$10$) [1–3]. To evaluate their current-carrying ability, various experiments have been carried out so far. In most cases, encouraging results have been obtained, such as a high J_c exceeding 10^5 A/cm^2 even under high-H above 10 T [4,5], a moderate anisotropy of J_c in superconducting tapes with respect to the direction of the applied H [6,7], and superior intergrain connectivity [8]. It was also demonstrated that the introduction of artificial pinning centers by irradiation with heavy ions, neutrons, electrons, etc., largely enhances J_c [9–12]. At the moment, the improvement of intergrain connectivity is one of the challenges for applications such as powder-in-tube wires and tapes [13,14]. At the same time, understanding of intragrain J_c properties and finding a way to enhance J_c are also important because the enhancement of the intragrain J_c leads to an extension of the operation temperature and field range.

From a basic point of view, Fe-based superconductors are layered materials, such as the cuprate high-T_c superconductors.

In the case of cuprates, vortices strongly interact with atomic-scale defects due to the short coherence length. The large magnetic penetration depth, the large anisotropy, and the high operation temperature amplify the effects of thermal fluctuations and give rise to unprecedented phenomena such as the elastic motion of the vortex lattice [15], plastic vortex motion [16,17], formation of a vortex glass [18], vortex melting [19], and an order-disorder phase transition [20–22] of the vortex lattice or its structural phase transition [23]. One naturally expects that the vortex physics of Fe-based superconductors is as rich as in the cuprate counterparts.

So far, intrinsic J_c properties of Fe-based superconductors and the relevant vortex physics have been investigated mainly on the following four systems: REFeAsO (where RE denotes rare-earth metal, 1111), AEFe$_2$As$_2$ (where AE denotes alkaline-earth metal, 122), AFeAs (where A denotes alkali metal, 111), and FeSe (11) -based compounds. Here most of the experiments were carried out on single-crystal samples and J_c was determined by magnetic hysteresis loop (MHL) measurements. To summarize the results, (1) J_c of Fe-based superconductors is generally high: $J_c \sim 2\,\text{MA/cm}^2$ at 5 K and 0 T for SmFeAsO$_{1-x}$F$_x$ [11], ~2 MA/cm^2 for K-Ba122 [24], ~0.1 MA/cm^2 for LiFeAs [25], and ~0.2 MA/cm^2 for FeTe$_{1-x}$Se$_x$ [26]. (2) The MHL measurements show a sharp peak at around zero field and a power-law decay of J_c at the low-field region, which are attributed to the strong pinning [27,28]. (3) The second magnetization peak (SMP) in the MHL, characterized by a hump far below H_{c2}, is evident in most cases, which supports a high J_c of Fe-based superconductors under high magnetic fields. As for the origin of the SMP, (i) a crossover from elastic creep to plastic creep [29–34] or (ii) the corresponding order-disorder transition of the vortex lattice [35,36] and (iii) a phase transition between a rhombic (at low H) and a high-H square vortex lattice [25,37,38], etc., have been put forth. (4) Various source of pinning were proposed. Examples are (i) dense vortex pinning nanostructures arising from inhomogeneous distributions of dopant atoms [39], (ii) charged dopant atoms [28], and (iii) structural/magnetic domain boundaries [40,41]. (5) Two kinds of pinning mechanism, namely, spatial variations in T_c (referred to as δT_c pinning) and fluctuations in the mean free path (δl pinning) [42] are discussed based on the T dependence of J_c [30,33,37,43–45]. (6) As for the doping dependence of J_c, existing results are controversial. For example, (i) the doping dependence of J_c follows the doping dependence of superconducting transition temperature (T_c) (for Co-Ba122 [30]), (ii) J_c does not follow T_c and becomes highest at the underdoped region (for Co-Ba122 [40] and K-Ba122 [46]), and (iii) J_c is determined by some extrinsic factors rather than by the doping concentration (for P-Ba122 [47]). At the moment a consensus has not been reached.

In order to understand the pinning mechanism of Fe-based superconductors and to find a way to enhance their J_c, the establishment of the doping dependence of J_c is useful, which enables us to discuss the relationship between J_c and system specific properties, such as T_c, H_{c2}, anisotropy, and dopant element. However, existing experimental results suggest that J_c of Fe-based superconductors also depends on extrinsic factors such as the quality of samples. Therefore, to deduce the inherent trends in behavior, systematic studies on various kinds of well-characterized samples are indispensable. For this purpose, 122 materials are most suitable for a number of reasons. First, high-quality single crystals with various doping elements (K for Ba, Co for Fe, and P for As) and with different doping concentration x are available. Second, 122-based compounds are the most promising candidates for practical applications among the known Fe-based superconductors [1–3] and any knowledge for enhancing J_c is therefore meaningful and valuable. This is one of the reasons why the pinning properties of 122 materials are investigated intensively.

In this study we carry out systematic experiments on the critical current properties in K-, Co-, and P-Ba122 using high-quality single crystals. This comparative study overviews the doping dependence of the critical current properties in these three materials, leading to a comprehensive understanding of the pinning mechanism in Fe-based superconductors. By examining a large number of samples, we successfully establish the doping dependence of J_c for the three cases. We demonstrate that J_c and the SMP effect significantly depend on the dopant elements and their concentrations. On the other hand, we find that J_c is largest for all dopants at the slightly underdoped composition, near the phase boundary between the SC phase and the antiferromagnetic-orthorhombic (AFO) phase. The sharp peak of J_c at a particular doping concentration is distinct from the T_c dome with a broad maximum. The scaling analysis of the normalized pinning force density [$f_p(h)$] shows that the peak position of $f_p(h)$ (h_{max}) takes a similar value of 0.40–0.45 for the highest-J_c samples, suggestive of a common mechanism that yields high J_c. The analysis of the T dependence of J_c indicates that the strength of both pinning mechanisms, δT_c pinning and δl pinning, is significantly larger in underdoped than in optimally or overdoped samples. These similarities found in the three cases indicate the presence of a common pinning source. Possible reasons for this enhanced pinning are discussed in detail.

The paper is organized as follows. In Sec. II we describe the experimental procedures. In Sec. III we show the T and H dependences of J_c for K-Ba122 (Sec. III A), Co-Ba122 (Sec. III B), and P-Ba122 (Sec. III C) with various x obtained from MHL measurements. Related physical properties, such as in-plane resistivity $\rho_{ab}(T)$ and $H_{c2}(T)$, are also presented. In Sec. IV the H dependence of the pinning force density and the T dependence of J_c are analyzed, and the possible source of pinning is discussed. In particular, we propose that δl pinning is responsible for the significantly enhanced J_c in highest-J_c K-Ba122 crystal. A summary is given in Sec. V.

II. EXPERIMENT

Single crystals of Ba$_{1-x}$K$_x$Fe$_2$As$_2$, Ba(Fe$_{1-x}$Co$_x$)$_2$As$_2$, and BaFe$_2$(As$_{1-x}$P$_x$)$_2$ were grown by the flux method using self-flux (KAs, FeAs, and Ba$_2$As$_3$/Ba$_2$P$_3$, respectively) following Refs. [48–50]. The compositions of the single crystals were determined by energy-dispersive x-ray (EDX) analysis and x-ray diffraction using Cu $K\alpha$ radiation. The c-axis lengths determined by x-ray diffraction were consistent with the compositions obtained from EDX. The samples were cut into rectangular shapes with typical dimensions

of $\sim$1–2 mm (length) $\times$ 0.5–1 mm (width) $\times$ 0.02–0.1 mm (thickness) for the magnetization $\chi(T)$ and the in-plane resistivity $\rho_{ab}(T)$ measurements. The T and H dependences of the magnetization $M(T,H)$ for $H \parallel c$ were measured using a magnetic property measurement system (Quantum Design). The $\rho(T)$ measurements were carried out by a standard four-probe method using a physical property measurement system (Quantum Design). For the estimation of J_c, we applied the Bean model [51], i.e.,

$$J_c = 20\Delta M/w(1 - w/3l),$$

where ΔM is the width of the MHL in the units of emu/cm^3, l is the sample length, and w is the sample width ($l > w$).

III. RESULTS

A. K-Ba122

1. Sample characterization

Figure 1(a) shows $\chi(T)$ for the K-Ba122 single crystals with their doping levels ranging from the underdoped ($x = 0.23$) to the overdoped ($x = 0.50$) region. To make the comparison easier, the data are normalized using the 5-K values. A sharp superconducting transition with a transition width ΔT_c of 0.5–1 K was observed except for $x = 0.23$ and 0.25 ($\Delta T_c \sim 2$–3 K). The T_c was defined as the midpoint of the transition and plotted as a function of x in Fig. 1(i). The T_c increases with x up to 38 K for $x = 0.36$ and decreases upon further doping down to 34 K at $x = 0.51$, thus forming a superconducting (SC) dome. The slope of the SC dome dT_c/dx

is $\sim$1.5 K per percent K on the underdoped side and –0.5 K per percent on the overdoped side. The broader transition of the underdoped samples might be associated with the larger slope, which causes a larger ΔT_c due to the spatial variation in x.

Figure 1(b) shows $\rho_{ab}(T)$ for K-Ba122 (top) and their differential curves $d\rho_{ab}/dT$ (bottom) below 150 K. For $x = 0.23$ and 0.25, $d\rho_{ab}/dT$ exhibits kink features at $T \sim$ 90 and 65 K as indicated by arrows, which correspond to the magnetostructural phase transition from the high-T paramagnetic-tetragonal (PT) phase to the low-T AFO phase [52]. The kink behavior is absent for $x = 0.29$ and above. The phase-transition temperatures $T_{s/N}$ are also plotted in Fig. 1(i).

Figures 1(c)–1(h) show $\rho_{ab}(T)$ of the $x = 0.23, 0.25, 0.29, 0.33, 0.36$, and 0.51 samples under magnetic fields $\mu_0 H = 0$–9 T applied parallel to the c axis (top) and to the ab plane (middle). The resistive transition at 0 T is sharp, with $\Delta T_c \sim 0.5$–1.0 K except for $x = 0.23$ ($\Delta T_c \sim 2$ K), and it shifts towards lower T at higher fields. Small but finite broadening is recognized with increasing H, particularly for $H \parallel c$. The upper critical fields along the c axis $H_{c2}^c(T)$ (squares) and along the ab plane H_{c2}^{ab} (triangles), defined by 90% of the normal-state resistivity, are plotted in the bottom panel. The slope dH_{c2}/dT was determined using data at $\mu_0 H \geqslant 1$ T, where $H_{c2}(T)$ is practically linear in T. The slope becomes highest at $x = 0.3$–0.4, with $dH_{c2}^{ab}/dT \sim 12$ T/K and $dH_{c2}^c/dT \sim 6.3$ T/K, respectively. For $x = 0.23$, the resistive transition occurs above T_c determined from $\chi(T)$, presumably due to the presence of higher-T_c segments arising
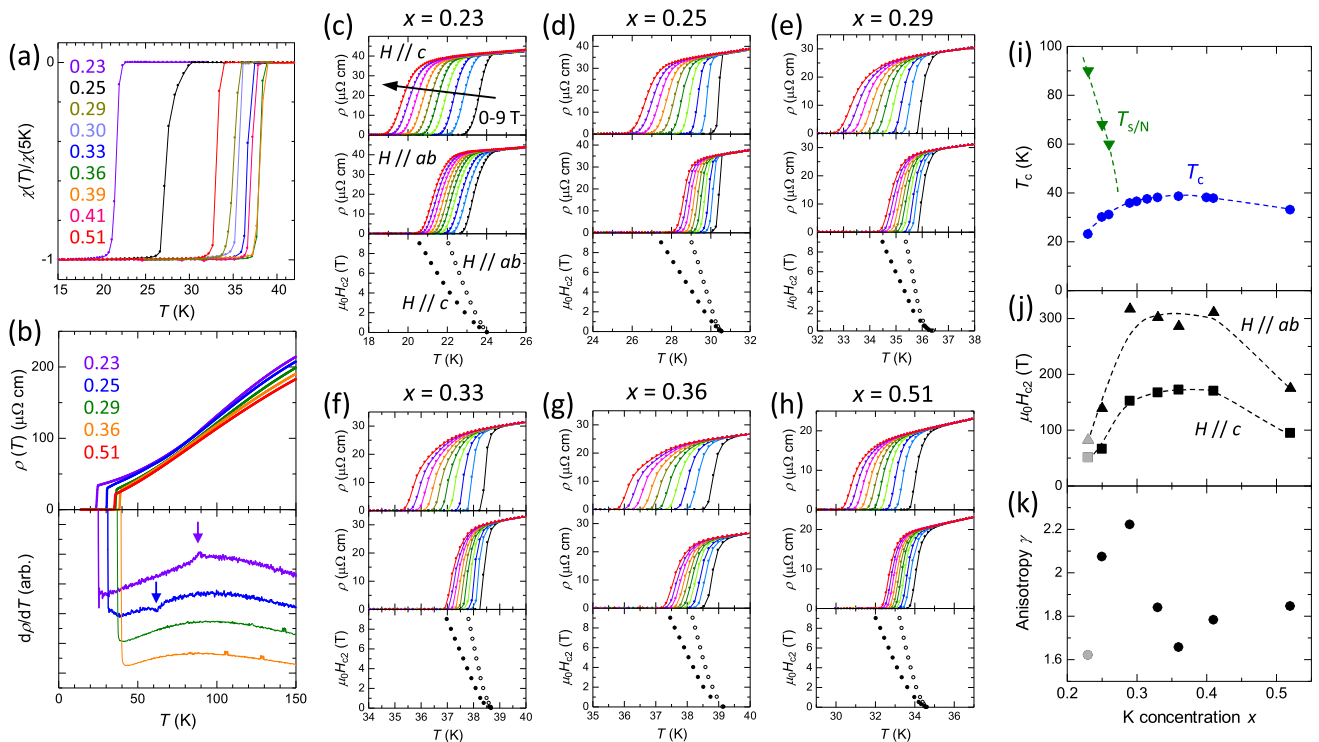

FIG. 1. Characterization of Ba$_{1-x}$K$_x$Fe$_2$As$_2$ single crystals with $x = 0.23$–0.51. (a) T dependence of magnetization. (b) T dependence of in-plane resistivity (top) and its derivative (bottom). (c)–(h) In-plane resistivity in magnetic fields parallel to the c axis (top) and ab plane (bottom). The bottom panel shows H_{c2} with $H \parallel c$ (closed circles) and ab (open circles) determined by 90% of normal state resistivity. (i)–(k) Doping dependence of T_c and $T_{s/N}$, $H_{c2}(0)$ for $H \parallel c$ (closed circles) and ab (open circles), and anisotropy γ of H_{c2} [$(dH_{c2}^{ab}/dT)/(dH_{c2}^c/dT)$].

from the spatial inhomogeneity of dopant elements. The H_{c2} at 0 K, $H_{c2}(0)$, was estimated by the extrapolation of the linear fit to $H_{c2}(T)$ and the Werthamer-Helfand-Hohenberg (WHH) formula $H_{c2}(0) = -0.69T_c(dH_{c2}/dT)$ [53]. The results are plotted in Fig. 1(j). The gray symbols indicate that the value may be overestimated owing to the broad resistive transition. Corresponding to the maximum T_c and the maximum dH_{c2}/dT slope, $H_{c2}(0)$ takes the maximum values of $\sim$170 T ($H \parallel c$) and $\sim$300 T ($H \parallel ab$) for $x = 0.3$–0.4 and rapidly decreases on both the underdoped and the overdoped sides. Figure 1(k) shows the anisotropy factor of H_{c2}, $\gamma = (dH_{c2}^{ab}/dT)/(dH_{c2}^{c}/dT)$, as a function of x. In the investigated temperature range, γ takes values 1.6–2.2 and does not show a noticeable x dependence. It should be noted that the WHH formula is valid for a superconductor in the clean limit with a single-band spherical Fermi surface and the obtained $H_{c2}(0)$ values are not quantitatively correct [in the present case, the $H_{c2}^{ab}(0)$ are overestimated]. In any case, the $H_{c2}(0)$ values of the present work are in good agreement with previous results, which have been also estimated by the WHH method [54]. This indicates that the quality of the present samples is good and resistivity measurement is properly done.

2. Magnetization hysteresis loops

The MHLs for $x = 0.23, 0.25, 0.29, 0.33, 0.36$, and 0.51 samples are shown in Figs. 2(a)–2(f) (5 K $\leqslant T \leqslant 0.7T_c$) and Figs. 2(g)–2(l) ($T \geqslant 0.7T_c$), respectively. The overall behavior of the MHL changes with x, which are classified into three groups, namely, group 1, of underdoped samples

($x = 0.23, 0.25$, and 0.30); group 2, of slightly underdoped sample ($x = 0.33$); and group 3, of optimally to overdoped samples ($x = 0.36$–0.51). Note that the shape of the MHL dramatically changes between $x = 0.30$ and 0.36, whereas T_c differs only by 1.5 K. In the following, the characteristics of the MHLs in these three groups are compared.

Group 1: underdoped samples ($x = 0.23, 0.25$, and 0.30). The MHL at $x = 0.23$ [Fig. 2(a)] is symmetric with respect to both H and M axes. This fact indicates that the dominant pinning mechanism is of bulk nature and thus justifies the application of the Bean model for the estimation of J_c. The H dependence of M is nonmonotonic. Following a sharp peak near $H = 0$, $M(H)$ decreases and then increases with H. The behavior is associated with the SMP, which enters into the measurement range ($\mu_0 H < 7$ T) above 10 K. The peak position, defined as H_{sp}, moves towards lower H with increasing T and persists up to $T = 20$ K [Fig. 2(g)]. The MHLs for $x = 0.25$ [Figs. 2(b) and 2(h)] and 0.30 [Figs. 2(c) and 2(i)] are qualitatively similar to the one for $x = 0.23$, while the magnitudes of M and H_{sp} are larger. The results are consistent with those reported by Yang *et al.* [24] and Kim *et al.* [55]

Group 2: slightly underdoped sample ($x = 0.33$). As shown in Figs. 2(d) and 2(j), the SMP effect is also present for $x = 0.33$. While the behavior is apparently similar to that in group 1 at low T, the MHLs at different T cross each other at high T [Fig. 2(j)]. This behavior implies that the $M(T)$ curve at fixed H exhibits a nonmonotonic T dependence, which possesses a peak at high T. Such a behavior does not occur in the group 1 samples, in which M monotonically decreases with T at any
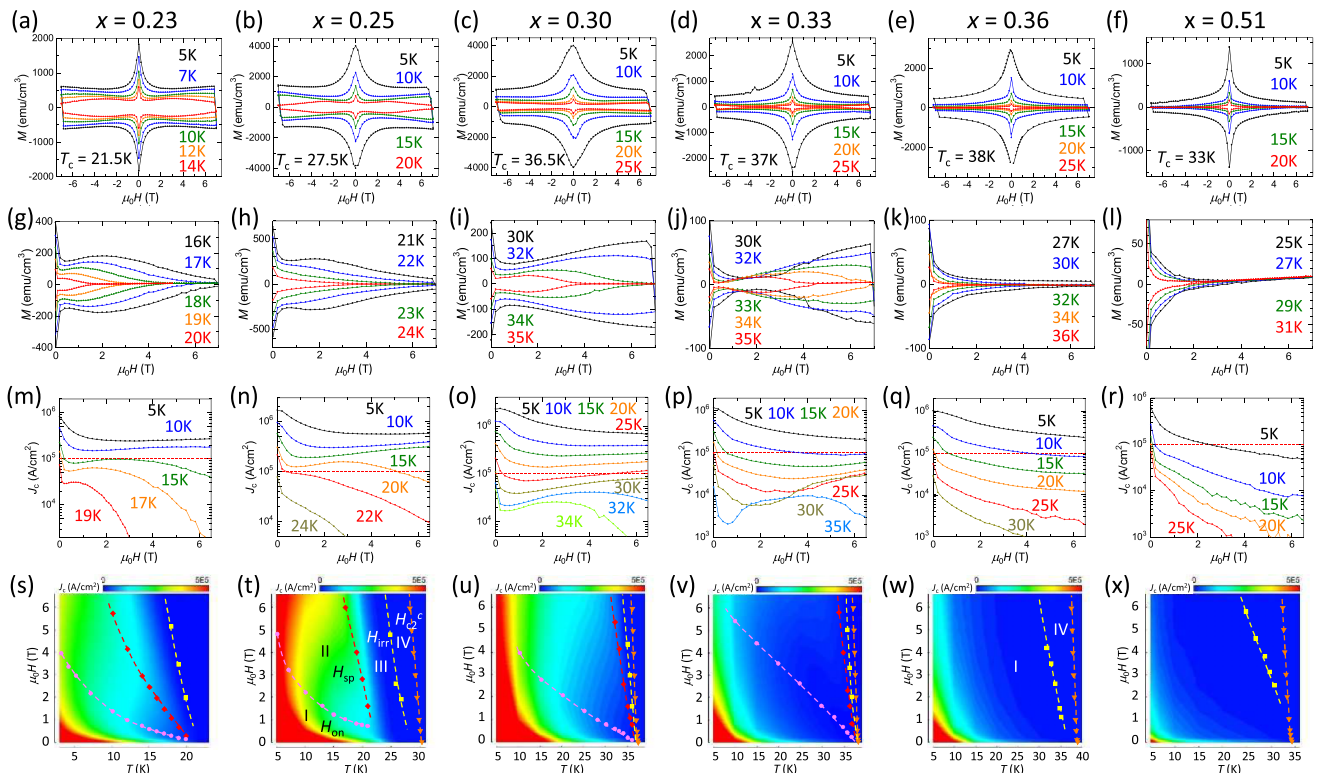

FIG. 2. Magnetization hysteresis loops for K-Ba122 samples with $x = 0.23, 0.25, 0.30, 0.33, 0.36$, and 0.51 at (a)–(f) $T \leqslant 0.7T_c$ and (g)–(l) $T \geqslant 0.7T_c$. (m)–(r) Magnetic field dependence of the critical current density for six samples. (s)–(x) Vortex phase diagram in the form of contour plots. Red (blue) color indicates the high-J_c (low-J_c) region.

H. Moreover, the magnitude of M decreases by nearly one order of magnitude compared to $x = 0.30$, even though their T_c are comparable. A similar SMP behavior is also observed in overdoped P-Ba122, which will be shown later.

Group 3: optimally doped to overdoped samples ($x = 0.36$–0.51). Here the width of the MHLs monotonically decreases with increasing H, in other words, the SMP effect is missing [see Figs. 2(e), 2(f), 2(k), and 2(l)]. As a consequence, the magnitude of M is small, particularly at high H. The disappearance of the SMP effect is unique to K-Ba122, not observed in Co- or P-Ba122 at any doping levels.

The present results indicate that the MHLs of K-Ba122 significantly depend on x. So far, some groups reported the existence of the SMP effect in optimally doped K-Ba122 [24,31], whereas other groups reported its absence [44,56]. The apparent discrepancy likely comes from a slight difference in the effective x.

3. Critical current density and vortex phase diagram

Based on the MHLs, we calculated J_c by employing the Bean model [51]. The results are shown in Figs. 2(m)–2(r). Here the y scales of these figures differ from each other. To make the comparison easier, red dashed straight lines mark $J_c = 0.1$ MA/cm^2 in the figures.

The group 1 samples, with $x = 0.23$ [Fig. 2(m)], $x = 0.25$ [Fig. 2(n)], and $x = 0.30$ [Fig. 2(o)], generally possess large J_c of the order of 0.1–1 MA/cm^2 over a wide T and H range. Among them, the largest J_c reaches 2.5 MA/cm^2 at $T = 5$ K and $\mu_0 H = 0$ T for the $x = 0.30$ sample. The H dependence of J_c is rather weak in these samples, which is due to the SMP effect existing at finite H.

J_c decreases for the group 2 ($x = 0.33$) sample [Fig. 2(p)]. The J_c of 1.2 MA/cm^2 at $T = 5$ K and $\mu_0 H = 0$ T is about half the one at $x = 0.30$. The $J_c = 0.01$ MA/cm^2 at $T = 30$ K and $\mu_0 H = 2$ T is one order of magnitude smaller than J_c for $x = 0.30$ under the same conditions, even though their T_c are almost the same.

For the group 3 samples, with $x = 0.36$ [Fig. 2(q)] and $x = 0.51$ [Fig. 2(r)], J_c monotonically decreases with H and its values become smaller, particularly at high T and high H. Above 20 K, J_c of the $x = 0.36$ sample is more than one order of magnitude smaller compared to $x = 0.30$. This result is rather unexpected since the crystal with $x = 0.36$ has the highest T_c among the K-Ba122 samples and is thus regarded as the optimal composition. For $x = 0.51$, J_c decreases by another order of magnitude, down to 0.001 MA/cm^2 at 20 K and 6 T, despite its T_c still being as high as 33 K. The co-occurrence of high T_c and low J_c in group 3 contrasts with low T_c and high J_c in the group 1 counterpart.

Figures 2(s)–2(x) show the T and H dependences of J_c in the form of contour plots. In the figures, several characteristic magnetic fields are also marked: H_{on}, the onset of the SMP effect defined by the local minimum of the MHL (pink circles); H_{sp}, the SMP position (red diamonds); H_{irr}, irreversibility field defined by a criterion of $J_c < 100$ A/cm^2 (yellow squares); and H_{c2}^c, the upper critical field along the c axis obtained from the resistivity measurements (orange triangles). These characteristic magnetic fields divide the superconducting state into four regions, namely, region I, below $H_{on}(T)$; region II,

between $H_{on}(T)$ and $H_{sp}(T)$; region III, between $H_{sp}(T)$ and $H_{irr}(T)$; and region IV, between $H_{irr}(T)$ and $H_{c2}(T)$.

For the group 1 samples, with $x = 0.23$ [Fig. 2(s)], $x = 0.25$ [Fig. 2(t)], and $x = 0.30$ [Fig. 2(u)], high-J_c areas, which are coded by bright colors, extend over a wide T and H range. Furthermore, it can be noticed that the red- and yellow-colored areas in Fig. 2(t) and the green- and light blue–colored areas in Fig. 2(u) fan out with increasing H. This behavior reflects the SMP effect. With increasing x, H_{sp} increases, resulting in the expansion of region II. In particular, for $x = 0.30$, region II dominates the superconducting phase, due to large H_{sp} even at high T. For $x = 0.25$ and 0.30, H_{irr} exists close to H_{c2}. This is consistent with the small broadening of $\rho_{ab}(T)$ and implies a weak thermal fluctuation, which is a favorable property for potential applications requiring a large current carrying ability. $H_{c2}(T)$ is not plotted for $x = 0.23$ [Fig. 2(s)], due to the uncertainty in determining $H_{c2}(T)$ from $\rho_{ab}(T)$ for this sample.

In the case of $x = 0.33$ [Fig. 2(v)], which is classified into group 2, the phase diagram is also divided into four regions reflecting the SMP effect. Here region I occupies a larger area and high J_c is realized within a limited space in region I, only at low T and low H. Indeed, in this case, region II is colored in blue, corresponding to $J_c < 0.1$ MA/cm^2. The facts indicate that the SMP does not lead to high J_c for $x = 0.33$, in contrast to group I.

For $x = 0.36$ [Fig. 2(w)] and $x = 0.51$ [Fig. 2(x)], the phase diagrams are separated into two regions, i.e., regions I and IV, due to the absence of the SMP. A high J_c is observed only at low-T and low-H regions as in the case of $x = 0.33$. For $x = 0.36$, $H_{irr}(T)$ is smaller compared with the $x = 0.30$ and 0.33 samples, while $H_{c2}(T)$ is almost identical for all compositions, leading to an expansion of region IV. This expansion is also recognized for $x = 0.51$. The small $H_{irr}(T)$ would suggest weak pinning, which will be discussed later.

The contour plots shown in Figs. 2(s)–2(x) are regarded as the vortex phase diagrams of K-Ba122. In general, the vortex phase diagram is determined by the competition of the elastic energy of the vortex lattice, the pinning energy, and the thermal energy. The SMP effect is commonly associated with an order-disorder transition, which occurs when the pinning energy exceeds the elastic energy. In previous studies of the 122-type Fe-based superconductors, two scenarios were proposed in discussing the vortex phase diagram associated with the SMP effect, namely, (i) the SMP is due to the crossover from the elastic creep to plastic creep [29–31] and (ii) the SMP comes from the structural phase transition of the vortex lattice [37,38]. Based on scenario (i), in regions I and II, the motion of the vortex is governed by the elastic creep, while it is governed by the plastic creep in region III. In this case, H_{sp} corresponds to the threshold field of the elastic-plastic crossover. Note that this scenario is compatible with the idea of an order-disorder transition, where H_{on} roughly corresponds to the onset of the transition. On the other hand, based on scenario (ii), H_{sp} corresponds to the phase transition field of the vortex lattice from the rhombic to the square structure. In region II, the vortex lattice softens as H approaches H_{sp}, and the vortices are pinned more easily, resulting in increasing J_c [57]. In the following we briefly examine whether and how one can explain the present results based on the above scenarios.

In general, J_c depends on the combination of two factors, namely, the elementary pinning force and the density of pinning centers. The pinning force is related to the condensation energy of a superconductor, since it determines the energy gain when the vortex core is located on the pinning centers. Since T_c and H_{c2} increase from $x = 0.23$ to 0.30, the increase in J_c in the group 1 samples can be attributed to the increase in the condensation energy. Here, both scenarios account for the observed x dependence. On the other hand, J_c decreases for $x = 0.33$ and 0.36 in spite of the increasing T_c and H_{c2}, which is unlikely to result for a decreasing condensation energy. One needs to assume that the density or the strength of the pinning centers significantly decreases from $x = 0.30$ to $x = 0.36$. The model of the order-disorder transition predicts that H_{on} and H_{sp} move closer to H_{irr} in this case [58], as experimentally observed. The crossing of MHLs at different T is often observed for comparatively small pinning when the peak position is already close to H_{irr}, as seen in $x = 0.33$ (group 2). If the pinning energy does not exceed the elastic energy in the entire field range, the SMP disappears, owing to the absence of the order-disorder transition as in the case for $x \geqslant 0.36$ (group 3). Thus, the doping evolution of the vortex phase diagram from group 1 to 3, in particular the monotonic increase of H_{on} with x, can be understood based on the order-disorder transition scenario by assuming a continuous weakening of pinning with increasing dopant concentration, which is consistent with the observed decrease in resistivity. Weak pinning also accounts for the lower H_{irr} (the expansion of region IV) for $x \geqslant 0.36$. The x dependence of the pinning behavior will be discussed quantitatively in Sec. IV.

4. Doping dependence of critical current density

Figures 3(a)–3(c) show $J_c(H)$ for $x = 0.23$–0.51 at $T = 5$ K, $T = 0.5T_c$, and $T = 0.8T_c$. Based on these results, we construct the contour plots of $J_c(x, H)$ in Figs. 3(d)–3(f). One can immediately find that the behavior in the underdoped ($x < 0.33$) region is distinct from the optimally doped and the overdoped ($x > 0.33$) counterpart. Below $x = 0.33$, high J_c is sustained up to $\mu_0H = 7$ T. Above $x = 0.33$, J_c decreases abruptly, especially in magnetic fields.

At $T = 0.5T_c$ [Fig. 3(e)], a local maximum in J_c occurs at 6 T for $x = 0.25$. This is due to the SMP effect. At $T = 0.8T_c$ [Fig. 3(f)], the composition with the highest J_c depends on H. Below $\mu_0H = 2$ T, the highest J_c is obtained at $x = 0.25$, while it shifts to $x = 0.30$ at higher fields $\mu_0H > 3$ T.

B. Co-Ba122

1. Sample characterization

Figure 4(a) shows the normalized $\chi(T)$ for Co-Ba122 single crystals with $x = 0.05, 0.057, 0.06, 0.08, 0.10$, and 0.12. A sharp superconducting transition with $\Delta T_c \sim 1$ K was observed, except for the underdoped ($x = 0.05$) and the heavily overdoped ($x = 0.12$) samples ($\Delta T_c \sim 2$–3 K). In Fig. 4(i), the x dependence of T_c is plotted: T_c increases with x up to $x = 0.06\,(T_c = 24$ K) and decreases with further doping, down to 11 K at $x = 0.12$. Here dT_c/dx is $\sim$12 K per percent Co on the underdoped side and $\sim$–2 K on the overdoped side. The magnitude of the slope is larger compared with K-Ba122 and P-Ba122 (shown later) on both sides.
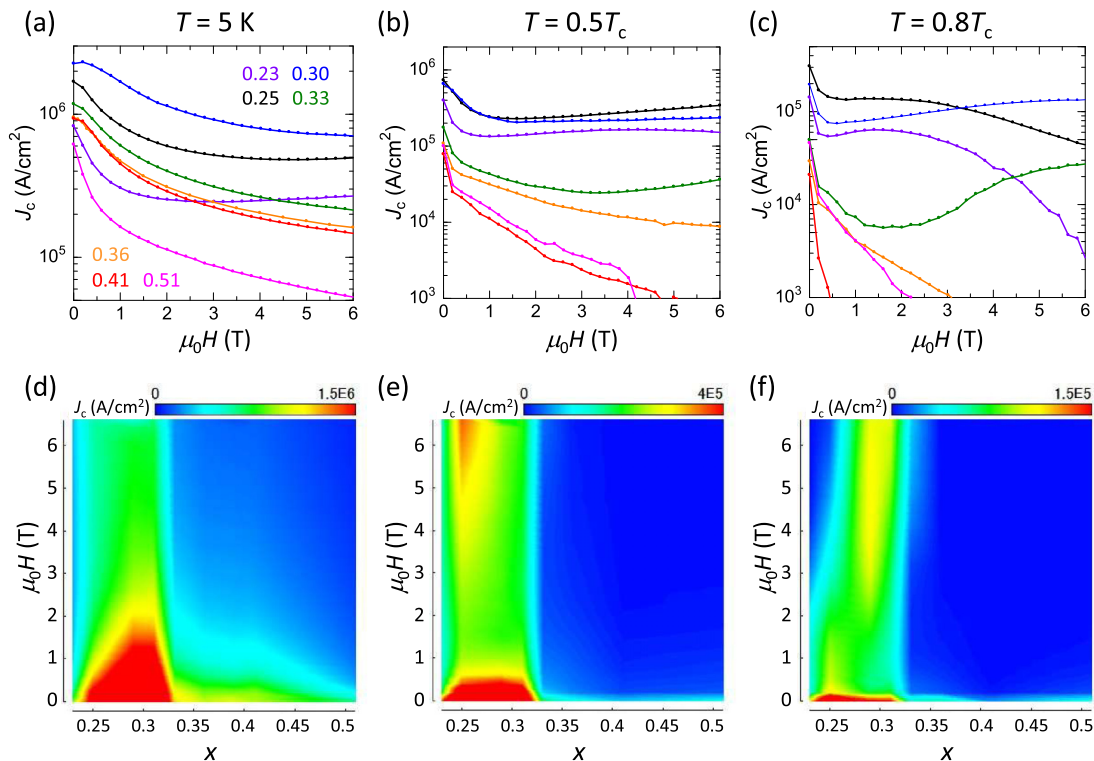

FIG. 3. (a)–(c) Magnetic field dependence of the critical current density for seven K-Ba122 samples at $T = 5$ K, $T = 0.5T_c$, and $T = 0.8T_c$. (d)–(f) Doping and field dependence of J_c derived from the top panels.
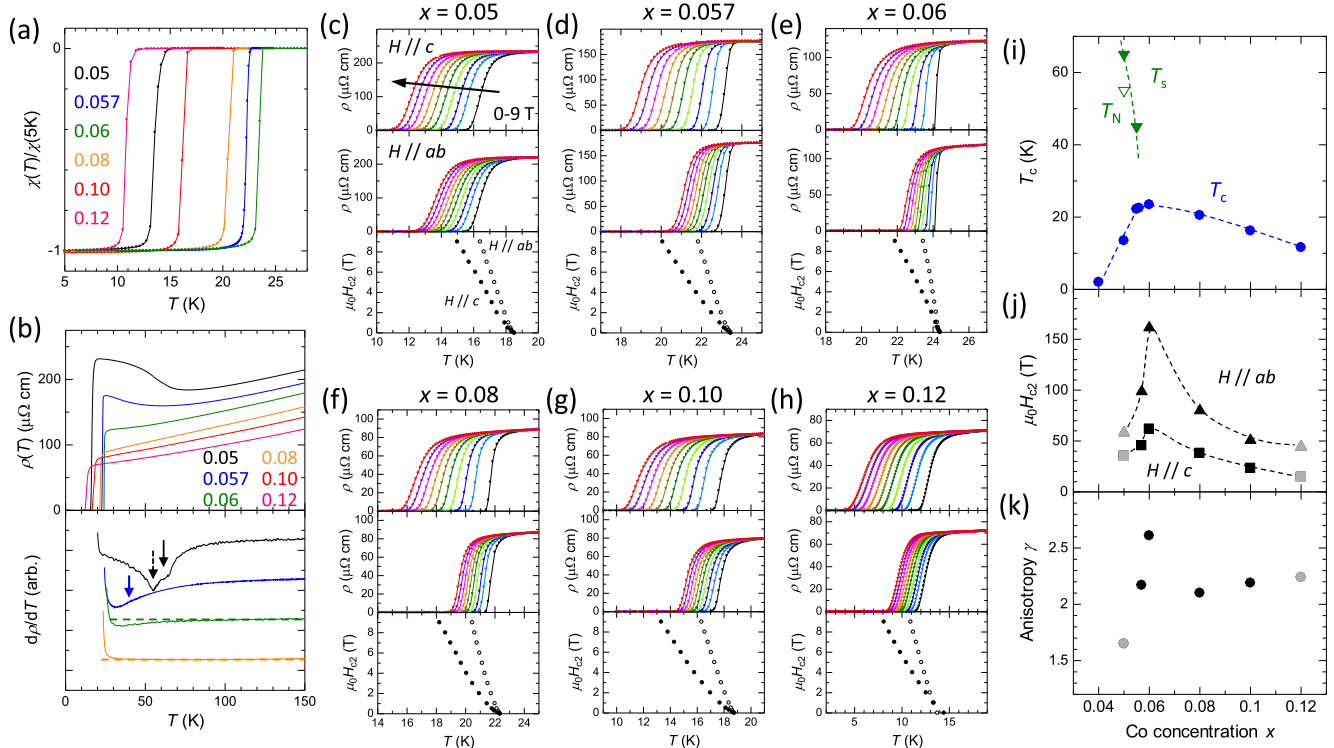
FIG. 4. Characterization of Ba(Fe$_{1-x}$Co$_x$)$_2$As$_2$ single crystals with $x = 0.05$–0.12. (a) Temperature dependence of magnetization. (b) Temperature dependence of in-plane resistivity (top) and the derivative (bottom). (c)–(h) In-plane resistivity in magnetic fields parallel to the c axis (top) and ab plane (bottom). The bottom panel show H_{c2}. (i)–(k) Doping dependence of T_c and $T_{s/N}$, $H_{c2}(0)$ with $H \parallel c$ (closed circles) and ab (open circles), and anisotropy γ of H_{c2} [$(dH_{c2}^{ab}/dT)/(dH_{c2}^c/dT)$].

Figure 4(b) shows $\rho_{ab}(T)$ (top) and $d\rho_{ab}/dT$ (bottom) below 150 K. For $x = 0.05$, $\rho_{ab}(T)$ shows an upturn at low T, which produces a shoulder and a dip in $d\rho_{ab}/dT$ at $T \sim 65$ and 55 K, respectively, as indicated by black arrows. They correspond to the structural (T_s) and the magnetic (T_N) phase transition temperatures, respectively [59,60]. For $x = 0.057$, the features in $d\rho_{ab}/dT$ are not clear. We define T_s as the temperature where the slope of $d\rho_{ab}/dT$ is largest, indicated by a blue arrow. For $x = 0.06$ and above, $\rho_{ab}(T)$ and $d\rho_{ab}/dT$ do not show an appreciable feature, suggesting that there is no phase transition. T_s and T_N are also plotted in Fig. 4(i).

Figures 4(c)–4(h) show $\rho_{ab}(T)$ of Co-Ba122 with $x = 0.05$–0.12 for $H \parallel c$ (top panels) and $H \parallel ab$ (middle panels). As in the case of K-Ba122, the resistive transition shifts towards low T with increasing H with a weak broadening. In the bottom panels, H_{c2}^c (closed circles) and H_{c2}^{ab} (open circles) are plotted. In addition, $H_{c2}(0)$ was estimated using the WHH formula and its x dependence is plotted in Fig. 4(j). Further, $H_{c2}(0)$ takes maximum values of 60 T for $H \parallel c$ and 150 T for $H \parallel ab$, respectively, at $x = 0.06$ and rapidly decreases along the underdoped ($x = 0.05$) and the overdoped ($x = 0.12$) sides. For $x = 0.05$ and 0.12, T_c defined by $\rho_{ab}(T)$ is higher than T_c defined by $\chi(T)$, thus the obtained $H_{c2}(0)$ values are overestimated ones. The data of the two samples are indicated by gray symbols. As shown in Fig. 4(k), γ takes values in the range of 1.7–2.7 and does not show a noticeable x dependence, similar to the case of K-Ba122.

2. Magnetization hysteresis loops

Figures 5(a)–5(l) show the MHLs for Co-Ba122 with $x = 0.05$–0.12 at selected T [Figs. 5(a)–5(f), 5 K $\leqslant T \leqslant 0.7T_c$; Figs. 5(g)–5(l), $T \geqslant 0.7T_c$]. In contrast to K-Ba122, all the MHL curves possess SMPs. For the most underdoped sample, with $x = 0.05$ [Figs. 5(a) and 5(g)], the MHL shows a symmetric shape with a sharp central peak. At 5 K [black curve in Fig. 5(a)], the SMP is located at $\mu_0 H_{sp} = 1.2$ T, moves to lower H with increasing T, and finally merges to zero field at $T \sim 8$ K. With increasing x, the SMP becomes evident, located at higher H. For example, for the optimally doped sample, with $x = 0.06$ [Figs. 5(c) and 5(i)], H_{sp} is located above 7 T at 5 K. With increasing T, H_{sp} moves to lower H, while it persists up to 22 K ($\sim 0.9T_c$). For the overdoped samples, wtih $x = 0.08$–0.12, the SMP feature is still evident [Figs. 5(d)–5(f) and 5(j)–5(l)]. Here H_{sp} decreases monotonically with increasing x, from $\mu_0 H_{sp} > 7$ T for $x = 0.08$ to $\mu_0 H_{sp} \sim 1.4$ T for $x = 0.12$ at 5 K. Correspondingly, the magnitude of M decreases with x.

3. Critical current density and vortex phase diagram

Figures 5(m)–5(q) show the calculated J_c at selected T for $x = 0.05$–0.12. The red dashed lines correspond to $J_c = 0.1$ MA/cm^2. Here J_c shows a similar H and T dependence, while the magnitude strongly depends on x. The largest $J_c = 1.2$ MA/cm^2 at $T = 5$ K and $\mu_0 H = 0$ T was recorded for the slightly underdoped ($T_c = 22.5$ K) sample with $x = 0.057$
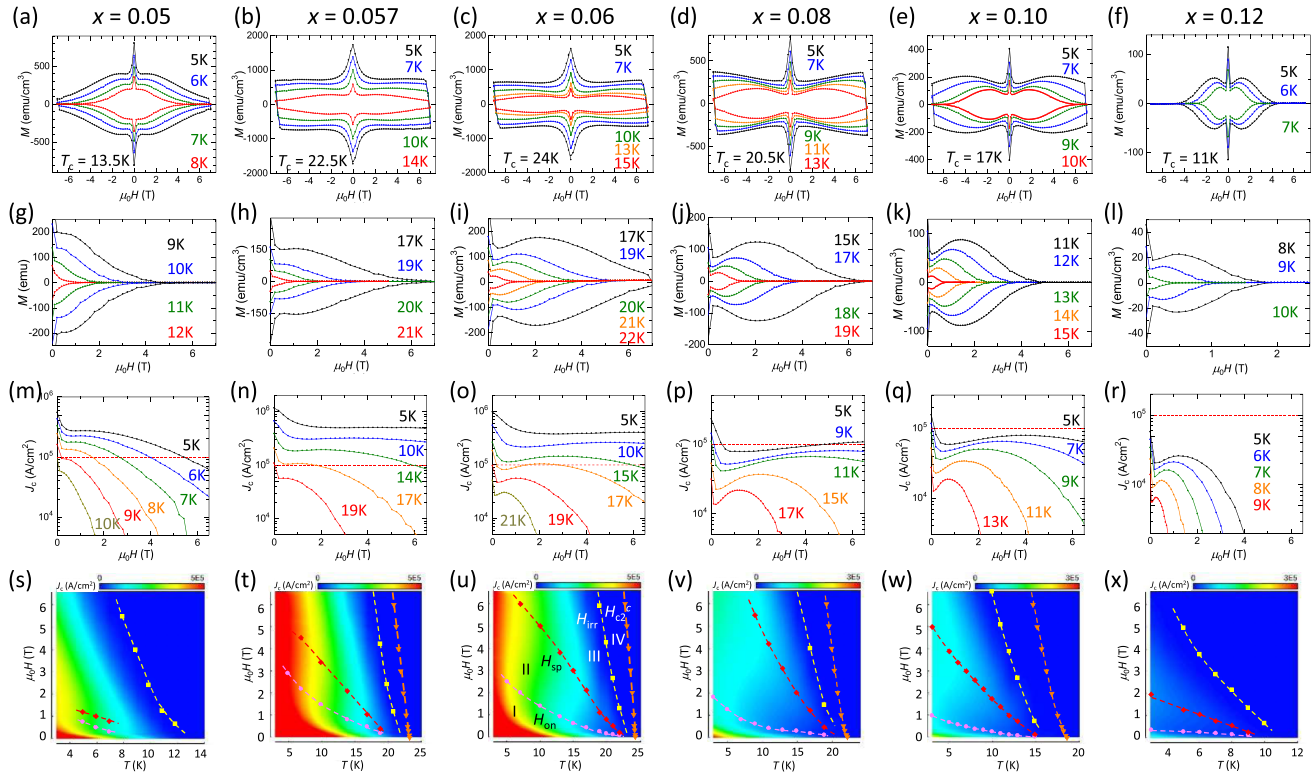
FIG. 5. Magnetization hysteresis loops for Co-Ba122 samples with $x = 0.05$, 0.057, 0.06, 0.08, 0.10, and 0.12 at temperatures (a)–(f) $T \leqslant 0.7 T_c$ and (g)–(l) $T \geqslant 0.7 T_c$. (m)–(r) Magnetic field dependence of the critical current density for six samples. (s)–(x) Vortex phase diagrams. Note that the color scale changes from $x \leqslant 0.06$ to $x \geqslant 0.08$.

[Fig. 5(n)]. In this sample, J_c exceeds 0.1 MA/cm^2 even under a high magnetic field of $\mu_0 H = 6$ T and up to a high temperature $T = 14$ K. A similarly large $J_c = 1.0$ MA/cm^2 ($T = 5$ K and $\mu_0 H = 0$ T) was also obtained for the optimally doped ($T_c = 24.0$ K) sample with $x = 0.06$ [Fig. 5(o)]. On the other hand, J_c of the overdoped samples significantly decreases. For $x = 0.08$ [Fig. 5(p)], J_c declines to 0.2 MA/cm^2 at $T = 5$ K and $\mu_0 H = 0$ T, which is one-fifth of the value for $x = 0.06$, while $T_c = 20.5$ K is relatively high. With further doping, J_c decreases to 0.06 MA/cm^2 for $x = 0.12$, which is one order of magnitude smaller than for the underdoped sample $x = 0.05$, even though the T_c of these two samples are comparable. A substantial degradation in J_c in the overdoped region is common to K- and Co-Ba122.

Figures 5(s)–5(x) display the T and H dependences of J_c by means of contour plots. Here the color scale changes from $x \leqslant 0.06$ to $x \geqslant 0.08$. We also plotted the characteristic magnetic fields H_{on} (pink circles), H_{sp} (red diamonds), H_{irr} (yellow squares), and H_{c2} (orange triangles). Because the SMP effect is seen in all the samples, the H-T contour maps are always separated into regions I–IV.

For $x = 0.05$ [Fig. 5(s)], H_{on} is located below 1 T and H_{sp} is about 0.5 T larger than H_{on}. Regions I and II cover a small area at low T and H. In this figure, $H_{c2}(T)$ is not plotted due to the uncertainty in the definition of H_{c2} from the resistivity data.

With x increasing to 0.057 [Fig. 5(t)], the high-current area expands to higher T and H. Also, H_{on} and H_{sp} increase compared with $x = 0.05$, resulting in the expansion of regions I and II. Here $H_{irr}(T)$ is close and nearly parallel to $H_{c2}(T)$, reflecting

the small resistive broadening. For $x = 0.06$ [Fig. 5(u)], H_{on} is similar to and H_{sp} is larger than for $x = 0.057$. As a result, region II is expanded and the high-J_c area extends up to high H along the H_{sp} line.

For $x = 0.08$ [Fig. 5(v)], the high-J_c region shrinks and the light blue region becomes dominant, corresponding to an abrupt decrease in J_c. On the other hand, H_{on} and H_{sp} do not show an appreciable difference compared to $x = 0.06$. With further doping to $x = 0.10$ [Fig. 5(w)] and $x = 0.12$ [Fig. 5(x)], the light blue region shrinks, reflecting a further decrease in J_c. Also, both H_{on} and H_{sp} become smaller (regions I and II shrink). For $x = 0.08$, $H_{c2}(T)$ is not plotted for the same reason as for $x = 0.05$.

4. Doping dependence of critical current density

Figures 6(a)–6(c) show $J_c(H)$ of Co-Ba122 with various x at $T = 5$ K, $T = 0.5 T_c$, and $T = 0.8 T_c$. The x dependence of J_c is visualized in Figs. 6(d)–6(f) by means of a contour plot. At 5 K [Fig. 6(d)], J_c rapidly increases with x and attains the maximum value at $x = 0.057$. Around $x = 0.057$–0.06, high J_c is sustained up to 7 T. Then J_c rapidly decreases toward $x = 0.08$. The light blue area extends at finite H in the overdoped region, which reflects the nonmonotonic H dependence of J_c due to the SMP effect. At $T = 0.5 T_c$ [Fig. 6(e)], J_c attains the maximum value at $x = 0.057$–0.06. Compared with $T = 5$ K, the light blue area moves to the lower-H region. For $T = 0.8 T_c$ [Fig. 6(f)], the light blue area further moves down to a lower-H region. Compared with K-Ba122, one can find a similarity that
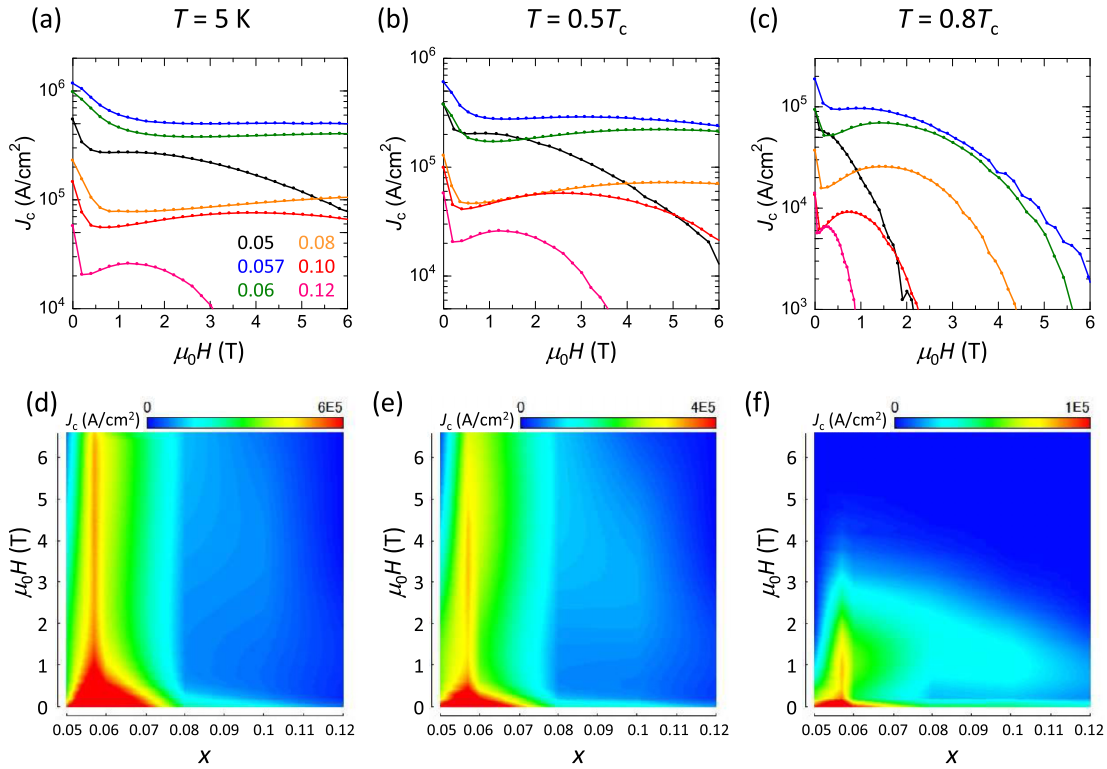
FIG. 6. (a)–(c) Magnetic field dependence of the critical current density for six Co-Ba122 samples at $T = 5$ K, $T = 0.5T_c$, and $T = 0.8T_c$. (d)–(f) Doping and field dependence of J_c derived from the top panels.

high-J_c values are attained in the underdoped side of the phase diagram and J_c rapidly decreases with overdoping. On the other hand, distinct from K-Ba122, the SMP exists over the entire x region, which fosters J_c at finite H.

For $0.05 \leqslant x \leqslant 0.06$, T_c and H_{c2} increase with x. In this sense, the doping evolution of J_c in the underdoped region can be attributed to the increase in the condensation energy, which leads to larger pinning force. On the other hand, J_c shows an abrupt decrease between $x = 0.06$ and 0.08, even though T_c and H_{c2} are almost the same. This suggests that the character of the pinning centers abruptly changes between $x = 0.06$ and 0.08.

C. P-Ba122

1. Sample characterization

Figure 7(a) shows the normalized $\chi(T)$ for the P-Ba122 single crystals with $x = 0.24, 0.30, 0.33, 0.38, 0.45,$ and 0.52. A sharp superconducting transition with $\Delta T_c \sim 0.5$–1.0 K is observed for the optimally doped and the overdoped samples ($x = 0.30$–0.45). The underdoped ($x = 0.24$) and the heavily overdoped ($x = 0.52$) samples show broader transitions ($\Delta T_c \sim 2$–3 K). Figure 7(i) shows the x dependence of T_c : T_c increases with x up to $x = 0.30$ ($T_c^{\max} = 29.5$ K) and decreases with further doping down to 15 K at $x = 0.52$. The x dependence of T_c is $dT_c/dx \sim 2$ K per percent P on the underdoped side and ~ -0.8 K on the overdoped side. These values are 50% larger than for K-Ba122, but three to six times smaller than for Co-Ba122.

Figure 7(b) shows $\rho_{ab}(T)$ (top) and $d\rho_{ab}/dT$ (bottom) below 150 K. A $\rho_{ab}(T)$ of $x = 0.24$ shows an upturn at $T \sim 60$ K. A dip in $d\rho_{ab}/dT$ exists at $T \sim 50$ K, as indicated by a black arrow, which corresponds to the PT-AFO phase transition. Also plotted in Fig. 7(i) is $T_{\mathrm{s/N}}$. For $x = 0.30$, such an anomaly is absent, while $\rho_{ab}(T)$ shows a slight deviation from the T-linear dependence below $T \sim 50$ K. For $x = 0.33$, $\rho_{ab}(T)$ shows a T-linear dependence for $T_c \leqslant T \leqslant 150$ K, which is often associated with the non-Fermi liquid charge transport, or quantum critical behavior [61,62].

Figures 7(c)–7(h) show $\rho_{ab}(T)$ for $H \parallel c$ (top panels) and $H \parallel ab$ (middle panels). The resistive transition is sharp ($\Delta T_c \sim 1$–2 K) except for $x = 0.24$, where $\Delta T_c \sim 8$ K. The transition shifts towards low T with increasing H without an appreciable resistive broadening. In the bottom panels, the T dependences of H_{c2}^c (closed circles) and H_{c2}^{ab} (open circles) are plotted. The $H_{c2}(0)$ for $H \parallel c$ and $H \parallel ab$ are estimated using the WHH formula and are plotted against x in Fig. 7(j). Note that H_{c2} for $x = 0.24$ may not reflect the intrinsic values owing to the very broad transitions and to the apparent higher T_c compared to that determined by $\chi(T)$. The values are marked in gray colors. Here H_{c2} takes a maximum value of 50 T for $H \parallel c$ and 110 T for $H \parallel ab$ at $x = 0.30$ and decreases along the underdoped ($x = 0.24$) and overdoped ($x = 0.52$) sides. The maximum H_{c2} is smaller than for K-Ba122 (170 T for $H \parallel c$ and 300 T for $H \parallel ab$) or Co-Ba122 (60 T for $H \parallel c$ and 150 T for $H \parallel ab$), while the maximum T_c of 29.5 K is intermediate between K-Ba122 ($T_c^{\max} = 38$ K) and Co-Ba122 ($T_c^{\max} = 24$ K). As shown in Fig. 7(k), γ takes values in the range of 1.6–2.5, again similar to K- and Co-Ba122.
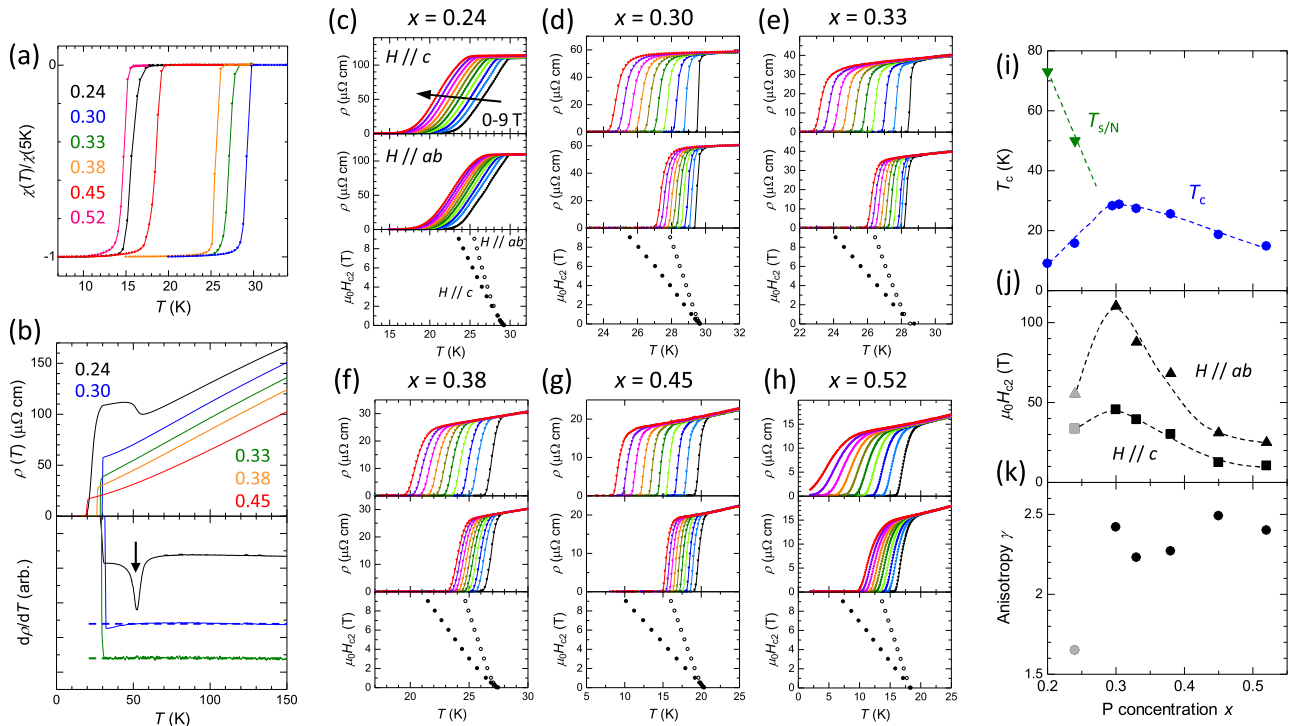
FIG. 7. Characterization of $BaFe_2(As_{1-x}P_x)_2$ single crystals with $x = 0.24$–0.52. (a) Temperature dependence of magnetization. (b) Temperature dependence of in-plane resistivity (top) and the derivative (bottom). (c)–(h) In-plane resistivity in magnetic fields parallel to the c axis (top) and ab plane (bottom). The bottom panels show H_{c2}. (i)–(k) Doping dependence of T_c and $T_{s/N}$, $H_{c2}(0)$ with $H \parallel c$ (closed circles) and ab (open circles), and anisotropy γ of H_{c2} [$(dH_{c2}^{ab}/dT)/(dH_{c2}^c/dT)$].

2. Magnetization hysteresis loops

Figures 8(a)–8(j) show the MHLs for P-Ba122 with $x = 0.24$–0.45 at selected temperatures [Figs. 8(a)–8(e), 5 K $\leqslant T \leqslant 0.7T_c$; Figs. 8(f)–8(j), $T \geqslant 0.7T_c$]. Here, depending on the overall features, we classify them into two groups, namely, group 1, consisting of underdoped and optimally doped samples ($x = 0.24$ and 0.30), where the magnitude of M shows a monotonic decrease with T at any H, in other words, the MHLs at different T do not cross each other, and group 2, consisting of overdoped samples ($x = 0.33$–0.45), where the MHLs at different T cross each other. In the following the characteristics of the MHLs in each x are compared.

In group 1, for $x = 0.24$ [Figs. 8(a) and 8(f)], the MHLs are symmetric with respect to M and H. At 5 K, a SMP is observed at $\mu_0 H_{sp} \sim 4$ T, which moves to lower H with increasing T and merges to the central peak at 9 K. For $x = 0.30$ [Figs. 8(b) and 8(g)], a clear SMP effect is observed, which persists up to $T = 28$ K $\sim 0.95T_c$. Compared with $x = 0.24$, the SMP is located at higher H. These behaviors are similar to underdoped K-Ba122 and Co-Ba122.

In group 2, for $x = 0.33$ [Figs. 8(c) and 8(h)], the MHLs at different T cross each other. With further doping, for $x = 0.38$ and $x = 0.45$, the shape of MHL becomes asymmetric with respect to the M axis. Indeed, for the $x = 0.45$ sample, at 13 K [black curve in Fig. 8(j)], M takes the minimum value at $\mu_0 H \sim 2$ T and shows a steplike increase at $\mu_0 H \sim 2.5$ T on the H-increasing branch, while M gradually decreases on the H-decreasing branch and takes its minimum at $\mu_0 H \sim 1.3$ T.

The above features are also seen in neutron-irradiated low-T_c superconductors such as V_3Si [63] and Nb [64], as well as in MgB_2 [65,66]. In these materials, weak pinning centers are introduced by the irradiation and the SMP is associated with the order-disorder transition of the vortex lattice. When the neutron fluence is low, MHLs look similar to those of group 2. With increasing neutron fluence, MHLs become similar to those of group 1. Based on the similar features of the MHLs, the SMP in P-Ba122 can also be associated with the order-disorder transition. For P-Ba122, based on the MHL measurements, Salem-Sugui *et al.* already proposed that the vortex lattice structural phase transition is the origin of the SMP [67]. If the order-disorder transition is indeed the case, the underlying mechanism of the SMP is different from the vortex lattice structural phase transition. Similar features were also seen in K-Ba122 for $x = 0.33$ [Fig. 2(j)], also classified as group 2.

So far, some groups reported the existence of the SMP effect [67,68], whereas other groups reported its absence [28,47]. In the latter cases, the MHLs were measured only in fields up to $\mu_0 H = 2$ T. According to the present results, it is difficult to observe the SMP effect below 2 T, which may be the reason for the apparent discrepancy.

3. Critical current density and vortex phase diagram

Figures 8(k)–8(o) show the calculated J_c for P-Ba122. The vertical scales differ from each other and red dashed lines correspond to $J_c = 0.1$ MA/cm^2. Here J_c strongly depends on x. For the underdoped crystal, with $x = 0.24$ [Fig. 8(k)], $J_c = 0.2$ MA/cm^2 was observed at $T = 5$ K
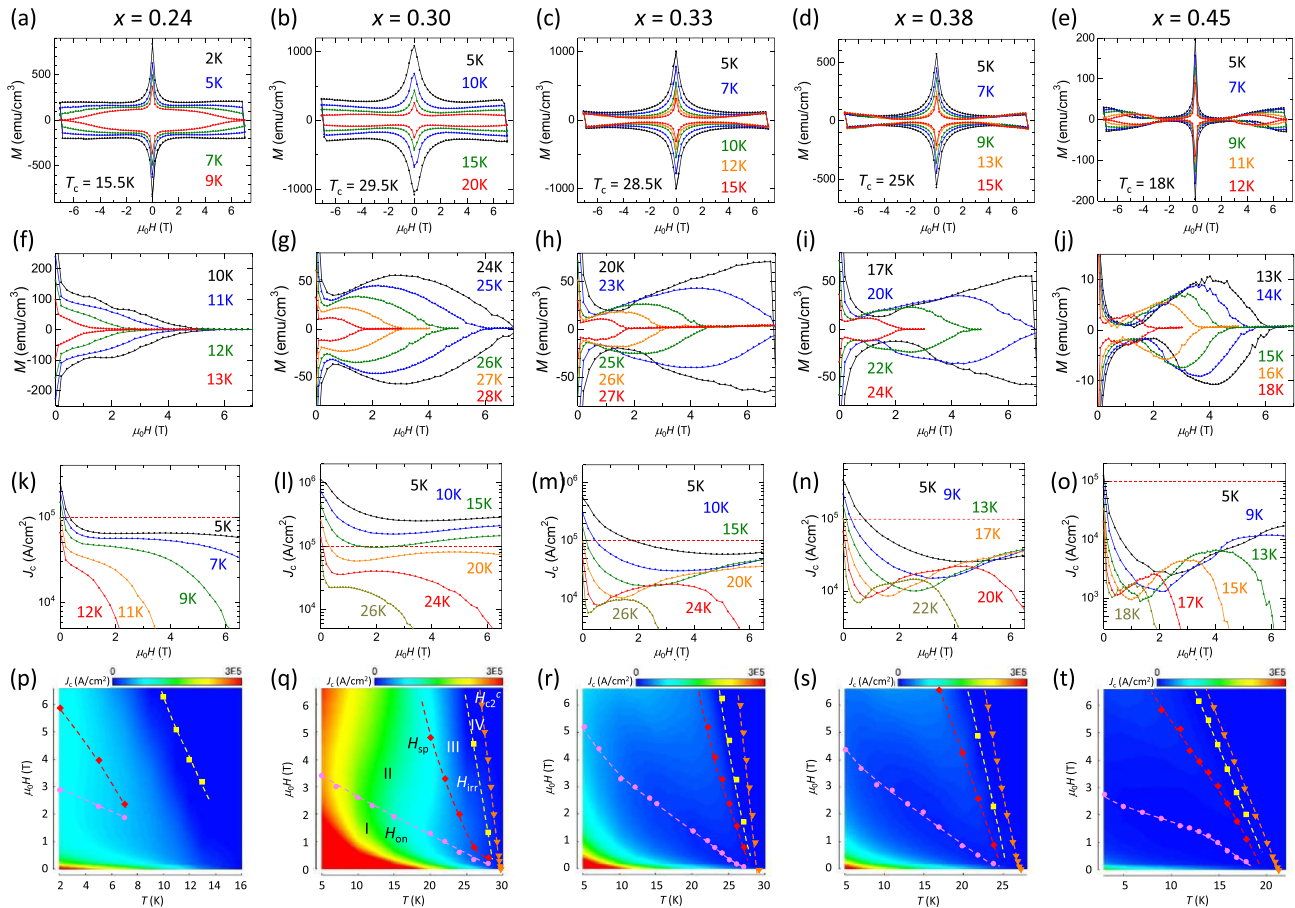
FIG. 8. Magnetization hysteresis loops for P-Ba122 samples with $x = 0.24$, 0.30, 0.33, 0.38, and 0.45 at (a)–(e) $T \leqslant 0.7T_c$ and (f)–(j) $T \geqslant 0.7T_c$. (k)–(o) Magnetic field dependence of the critical current density for six samples. (p)–(t) Vortex phase diagrams.

and $\mu_0 H = 0$ T. Further, J_c rapidly falls off with increasing H, below 0.1 MA/cm^2, even at $T = 5$ K and $\mu_0 H = 0.5$ T. The largest $J_c = 1.0$ MA/cm^2 ($T = 5$ K and $\mu_0 H = 0$ T) was achieved for $x = 0.30$ [Fig. 8(l)]. For P-Ba122, only this composition sustains high-J_c values under magnetic fields up to high T. Here J_c abruptly decreases from $x = 0.30$ (group 1) to 0.33 (group 2), while T_c decreases only by 1 K. As shown in Fig. 8(m), $J_c = 0.5$ MA/cm^2 at $T = 5$ K and $\mu_0 H = 0$ T is about half of that for $x = 0.30$. Furthermore, at $T = 5$ K and $\mu_0 H = 6$ T, $J_c = 0.06$ MA/cm^2 is one-fifth of that for $x = 0.30$. With further doping, for $x = 0.38$ and 0.45 [Figs. 8(n) and 8(o)], J_c becomes even smaller.

Figures 8(p)–8(t) show the T and H dependences of J_c by means of contour plots. The characteristic fields H_{on} (pink circles), H_{sp} (red diamonds), H_{irr} (yellow squares), and H_{c2} (orange triangles) are also plotted. Because all MHLs exhibit the SMP effect, the H-T contour maps are separated into regions I–IV for all x.

For $x = 0.24$ [Fig. 8(p)], a relatively high-J_c (light blue) area covers only the low-T region. Here $H_{c2}(T)$ is omitted owing to the broad resistive transition. For $x = 0.30$ [Fig. 8(q)], a high-J_c area extends over a wide T and H range. Here H_{sp} is larger compared with $x = 0.24$, which results in the increase of region II, also producing a high-J_c area around it up to high H. Region IV covers a narrow area, reflecting that H_{irr} and H_{c2} are close to each other.

For $x = 0.33$ shown in Fig. 8(r), H_{sp} line lies closer to H_{irr}, possibly reflecting the decrease in the pinning energy. Region II does not support high J_c. With further doping, the phase diagrams of $x = 0.38$ [Fig. 8(s)] and 0.45 [Fig. 8(t)] are dominated by the low-J_c (blue color) area except for zero field. H_{sp} locates close to H_{irr}, which, according to the order-disorder transition model, suggests a further decrease in the pinning energy with overdoping.

4. Doping dependence of critical current density

Figures 9(a)–9(c) show $J_c(H)$ of P-Ba122 with various x at $T = 5$ K, $T = 0.5T_c$, and $T = 0.8T_c$, respectively. The x dependence of J_c is visualized in Figs. 9(d)–9(f) by means of a contour plot. At 5 K [Fig. 9(d)], starting from $x = 0.24$, J_c increases with x and attains the maximum value at $x = 0.30$. Around $x = 0.30$, high J_c is sustained up to 7 T; J_c rapidly decreases toward $x = 0.33$. At $T = 0.5T_c$ [Fig. 9(e)], the light blue area emerges at high $\mu_0 H \sim 6$ T in the overdoped region, reflecting the SMP located close to H_{irr}. For $T = 0.8T_c$ [Fig. 9(f)], the light blue area moves down to the lower-H region.

D. Doping dependence of J_c for three cases

Figures 10(a)–10(f) summarize the x dependence of J_c for K-, Co-, and P-Ba122 at $\mu_0 H = 0.4$ T [Figs. 10(a)–10(c)] and
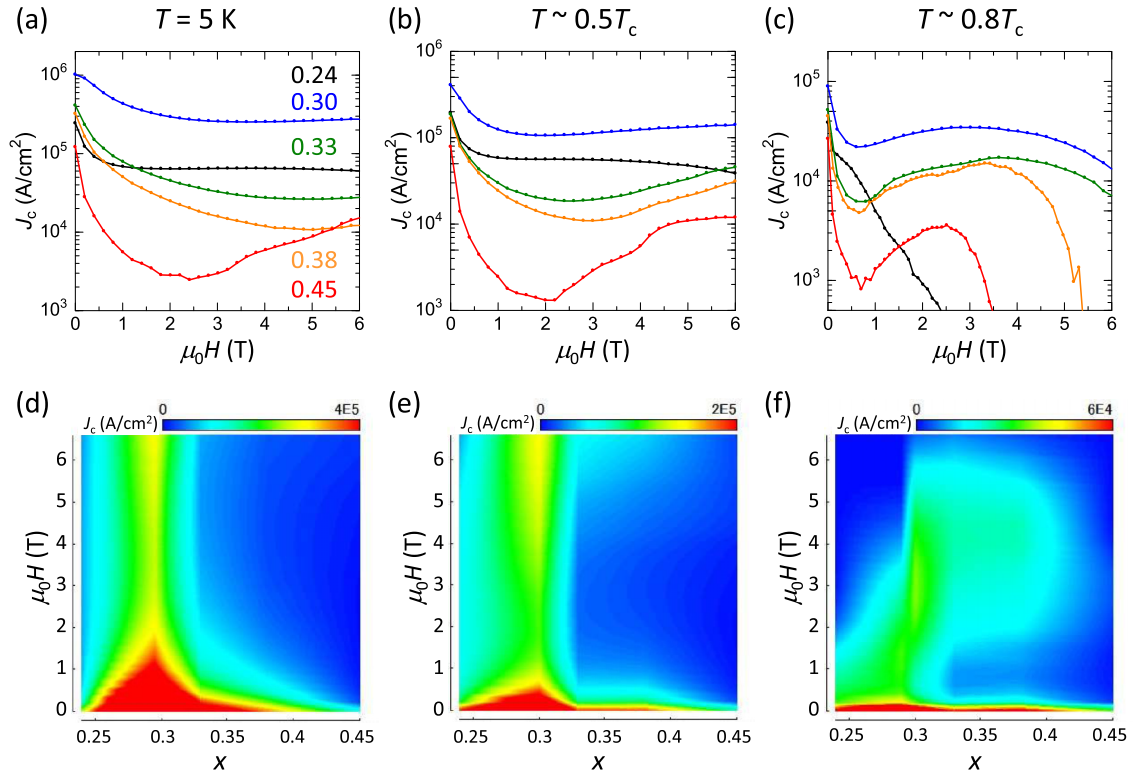
FIG. 9. (a)–(c) Magnetic field dependence of the critical current density for five P-Ba122 samples at $T = 5$ K, $T = 0.5T_c$, and $T = 0.8T_c$. (d)–(f) Doping and field dependence of J_c derived from the top panels.
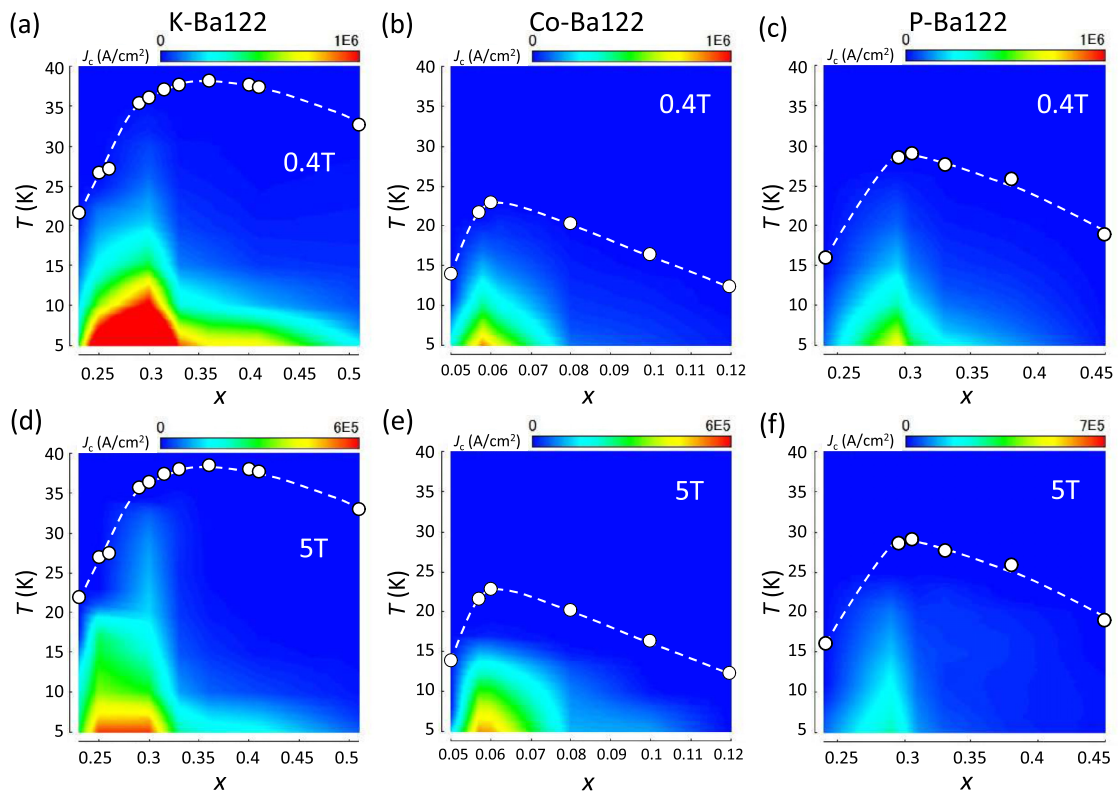

FIG. 10. Doping and temperature dependence of the critical current density (measured at $\mu_0 H = 0.4$ T and 5 T) for (a), (d) $Ba_{1-x}K_xFe_2As_2$, (b), (e) $Ba(Fe_{1-x}Co_x)_2As_2$, and (c), (f) $BaFe_2(As_{1-x}P_x)_2$. The T_c-x curves are also plotted in each panel.

5 T [Figs. 10(d)–10(f)] in the form of contour plots. In the same figures, the T_c are also plotted using open circles. Here the red regions correspond to $J_c \geqslant 1$ MA/cm^2 in Figs. 10(a)–10(c) (0.4 T) and $J_c \geqslant 0.7$ MA/cm^2 in Figs. 10(d)–10(f) (5 T). In general, K-Ba122 possesses higher J_c compared with Co- and P-Ba122. At $\mu_0 H = 0.4$ T, the highest J_c of 2.6 MA/cm^2 at 5 K is achieved in K-Ba122 at $x = 0.30$. Co-Ba122 possesses the highest J_c of 0.9 MA/cm^2 at $x = 0.057$, being a little bit above the highest J_c of P-Ba122, 0.7 MA/cm^2 at $x = 0.30$. The same tendency is observed at higher field $\mu_0 H = 5$ T; the highest J_c values at 5 K are 0.7 MA/cm^2 in K-Ba122 ($x = 0.30$), 0.5 MA/cm^2 in Co-Ba122 ($x = 0.057$), and 0.2 MA/cm^2 in P-Ba122 ($x = 0.30$). Judging from J_c of the pristine single-crystal samples, K-Ba122 is superior to P- and Co-Ba122 as a candidate material for applications.

Common to the three doping variations, J_c increases with x from the underdoped to the optimally doped region, apparently following the increase in T_c. With further doping, J_c rapidly decreases above critical doping levels, $x_c \sim 0.30$ for K-Ba122, ~ 0.06 for Co-Ba122, and ~ 0.30 for P-Ba122. Figures 10(a) and 10(d) also confirm that for K-Ba122, the x dependence of J_c is distinct from that of T_c. For Co- and P-Ba122, the highest J_c is realized nearly at the highest-T_c compositions, $x \sim 0.06$ for Co-Ba122 and $x \sim 0.30$ for P-Ba122. However, on the overdoped side of the phase diagram, J_c decreases more rapidly in contrast to the weak decrease in T_c, as indicated by the large blue areas spreading in the overdoping regions. In this regard, the doping dependence of J_c does not simply follow T_c in all three cases.

IV. DISCUSSION

A. Magnetic field dependence of pinning force density

In this section, in order to gain insight into the pinning mechanism, we analyze the pinning force density, defined as $F_p = J_c \mu_0 H$. Figure 11 shows the pinning force density normalized to its maximum value, namely, $f_p = F_p / F_p^{max}$ is plotted against the reduced magnetic field, $h = H/H_{irr}$, for K-Ba122 [Figs. 11(a)–11(d)], Co-Ba122 [Figs. 11(f)–11(i)], and P-Ba122 [Figs. 11(k)–11(n)]. For most samples, H_{irr} exceeds the accessible magnetic field of 7 T at low T. In such cases only data referring to high T are presented. In general, $f_p(h)$ follows the functional form $f_p(h) = Ah^p(1-h)^q$, where A is a constant and p and q are parameters providing information of the pinning mechanism [69]. If pinning is governed by a single mechanism within a certain T range, the $f_p(h)$ at different T collapse into one master curve, in other words, scaling of $f_p(h)$ as a function of h is expected. It should be mentioned that the Dew-Hughes model [69] is based on purely geometric arguments neglecting the elasticity of the vortex lattice. This means that it is valid in a plastically deformed lattice only and in principle inappropriate for discussing the pinning mechanisms in samples showing the SMP, where the elastic and pinning energies are comparable and effectively compete with each other. In particular, the position of the SMP resulting from an order-disorder transition of the vortex lattice is a function of the defect density (or pinning force) and even not necessarily constant in temperature [58]. A shift of the maximum in J_c obviously results in a shift of the maximum

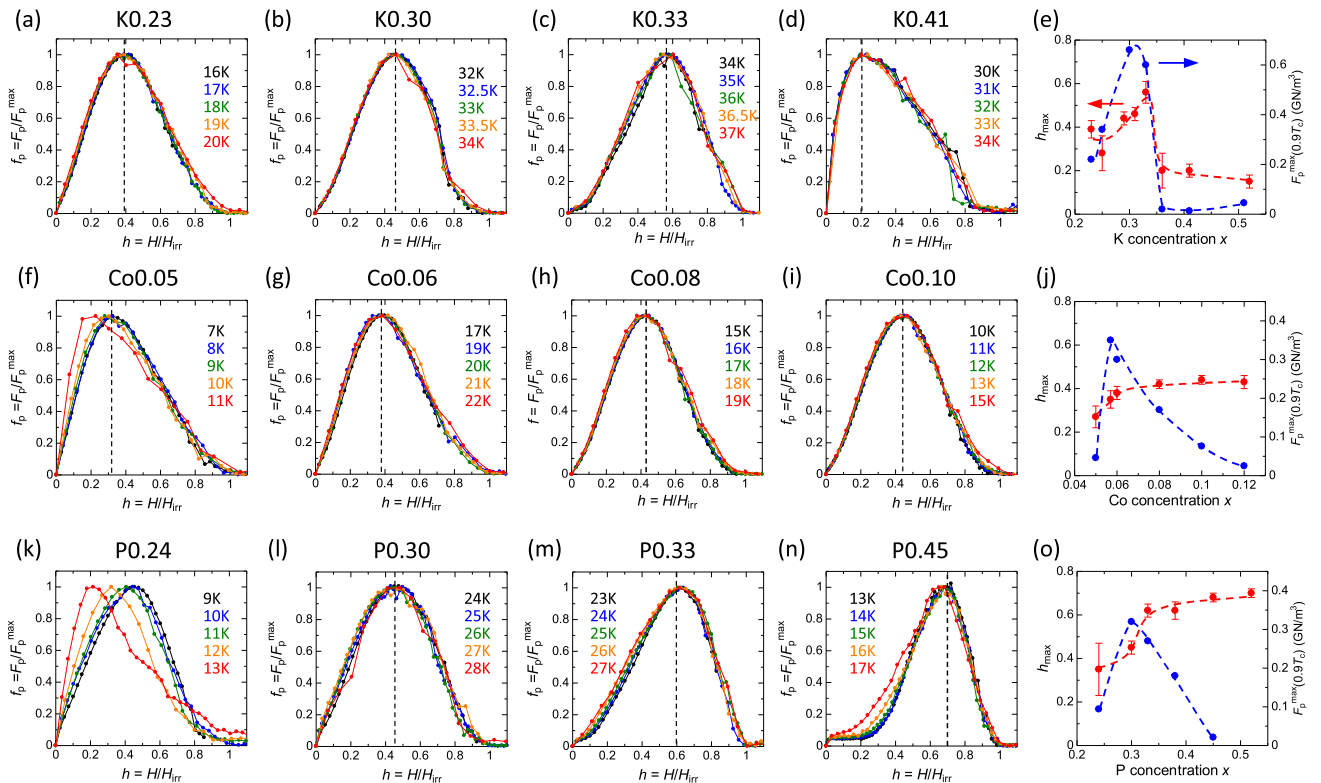FIG. 11. Normalized pinning force density ($f_p = F_p / F_p^{max}$) plotted against the reduced magnetic field ($h = H/H_{irr}$) for (a)–(d) K-Ba122, (f)–(i) Co-Ba122, and (k)–(n) P-Ba122. Also shown are the x dependences of h_{max} and $F_p^{max}(0.9T_c)$ for (e) K-Ba122, (j) Co-Ba122, and (o) P-Ba122.

in the pinning force; thus the peak of f_p can be at different positions irrespective of the pinning mechanism. However, this kind of analysis is frequently done in the literature and we will apply it to our data for the sake of comparison with the literature and between the different samples. While a universal form of f_p at various temperatures is certainly a strong indication of one underlying pinning mechanism, a shift of the peak is not necessarily caused by a change of the pinning mechanism.

Figures 11(a)–11(d) show $f_p(h)$ for K-Ba122 with $x = 0.23, 0.30, 0.33$, and 0.41, respectively. For $x = 0.23$ [Fig. 11(a)], $f_p(h)$ between 16 and 20 K lie on a single curve, indicating that a single pinning mechanism plays a dominant role within this T range. At $h_{max} \sim 0.39$, $f_p(h)$ exhibits a peak. For $x = 0.30$ [Fig. 11(b)], which possesses the highest J_c, the peak position h_{max} shifts to ~0.46, suggesting a change in the dominant pinning mechanism or a reduction of the defect density ρ_D. In addition, h_{max} becomes larger, up to 0.56 for $x = 0.33$ [Fig. 11(c)], likely due to a further reduction of ρ_D, and then suddenly decreases down to 0.20 for $x = 0.41$ [Fig. 11(d)]. The latter change is associated with the disappearance of the SMP effect; pinning is too weak to disorder the flux line lattice at high fields. The x dependence of h_{max} is shown in Fig. 11(e) together with the x dependence of F_p^{max} at $T = 0.9T_c$. Apparently, the x dependence of h_{max} correlates with that of $F_p^{max}(0.9T_c)$ and highlights the sudden change in pinning that occurs between $x = 0.33$ and 0.36. The present results are consistent with previous reports [24,41].

Figures 11(f)–11(i) show $f_p(h)$ for Co-Ba122 with $x = 0.05, 0.06, 0.08$, and 0.10. For $x = 0.05$ [Fig. 11(f)], $f_p(h)$ shows a reasonable scaling behavior with $h_{max} \sim 0.32$ at low T between 7 and 9 K. However, at 10 and 11 K, $f_p(h)$ deviates from the scaling behavior, suggesting that different pinning mechanisms are at work. In the case of $x = 0.06$ [Fig. 11(g)], a scaling behavior is observed above 17 K ($\sim 0.7T_c$). Here h_{max} is 0.38, which is similar to but slightly larger than that of $x = 0.05$. A similar scaling behavior is observed for the overdoped samples, with $x = 0.08$ [Fig. 11(h)] and $x = 0.10$ [Fig. 11(i)], with $h_{max} = 0.42$–0.44. The x dependence of h_{max} and $F_p^{max}(0.9T_c)$ are plotted in Fig. 11(j). Besides the heavily underdoped region ($x \sim 0.05$), h_{max} shows weak x dependence, suggesting that the relevant pinning landscape does not change with x. Presumably related to the constant h_{max}, the x dependence of $F_p^{max}(0.9T_c)$ is rather gradual, in contrast to K-Ba122 in which both F_p^{max} and h_{max} significantly change with x.

The $f_p(h)$ for P-Ba122 with $x = 0.24, 0.30, 0.33$, and 0.45 are shown in Figs. 11(k)–11(n). For $x = 0.24$ [Fig. 11(k)], h_{max} changes with T, from $h_{max} = 0.45$ at 9 K to $h_{max} = 0.2$ at 13 K. The behavior resembles that for Co-122 with $x = 0.05$ [Fig. 11(f)] and indicates that the dominant pinning source changes with T. For $x = 0.30$ [Fig. 11(l)], the scaling behavior prevails between 17 and 22 K with $h_{max} = 0.45$. The same h_{max} value is obtained also for $x = 0.24$ at low T, presumably suggesting the same pinning sources. For $x = 0.33$ [Fig. 11(m)], the scaling is demonstrated between 23 and 27 K. Here h_{max} increases up to 0.62, indicative of a weakening in the pinning, consistent with the decrease of F_p^{max}. Then h_{max} further increases up to 0.7 for $x = 0.45$ [Fig. 11(n)] and the peak width becomes narrower, consistent with both the

order-disorder scenario and a pinning structure, which can disorder the vortex lattice only close to H_{irr}. Furthermore, at $T > 16$ K, an extra feature appears at the low-h region. The present observations, namely, multiple features in $f_p(h)$ and large $h_{max} \sim 0.7$, are in good agreement with the report by Fang *et al.* [68] The x dependences of h_{max} and $F_p^{max}(0.9T_c)$ are plotted in Fig. 11(o). The x dependence of h_{max} in P-Ba122 resembles the neutron-fluence dependence of h_{max} in neutron-irradiated superconductors, which can be understood in terms of the order-disorder transition with different density of pinning centers.

Through the comparison of $f_p(h)$ for K-, Co-, and P-Ba122, several similarities and differences can be pointed out. (1) For underdoped Co-Ba122 [Fig. 11(a)] and P-Ba122 [Fig. 11(k)], scaling behavior is violated at high T. This may indicate the existence of multiple pinning sources that become dominant at different T. (2) For the optimally doped samples, scaling behavior prevails at least at high T. In addition, h_{max} tends to increase with increasing x and the highest J_c is attained when h_{max} becomes 0.40–0.45, at $x = 0.30$ for K-Ba122 [Fig. 11(b)], $x = 0.06$ for Co-Ba122 [Fig. 11(g)], and $x = 0.30$ for P-Ba122 [Fig. 11(l)]. The coincidence suggests that the highest J_c is caused by the same pinning mechanism(s) common to the three samples. (3) In the overdoped region, $f_p(h)$ behaves differently [Figs. 11(d), 11(i), and 11(n)]. This suggests that the dominant pinning mechanism that produces high J_c disappears in the overdoped region and other pinning mechanisms that are more specific to the dopant variation are at work.

The scaling analysis presented above suggests that a single pinning mechanism is dominant over a certain T range. As stated, however, one should keep in mind that the scaling analysis can be accurately performed only if H_{irr} is well defined. At low T, H_{irr} exceeds the upper limit of the accessible magnetic field of 7 T and therefore it is not clear at this moment whether there exist extra pinning mechanisms at lower T. Violation of the scaling behavior in the underdoped and overdoped Co-Ba122 and P-Ba122 indeed suggests the existence of multiple pinning sources. In the next section we investigate the T dependence of J_c in order to complement the x and T dependences of the pinning mechanism.

B. Temperature dependence of J_c

In discussing the T dependence of J_c, one should consider two distinct contributions, i.e., strong pinning and weak collective pinning. The strong pinning comes from sparse and large (nanometer-sized) heterogeneities, while the weak collective pinning is related to dense, small (atomic-scale) pinning centers. Several results indicate the existence of strong pinning. For example, small-angle neutron scattering [70], Bitter decoration [71], magnetic force microscopy [70], and scanning tunneling microscopy [72] studies revealed a disordered vortex lattice. Here the vortex lattice is expected to be highly disordered because each vortex is preferentially pinned by the sparse, randomly distributed pinning sites. Also, the MHL measurements show a sharp peak at around zero field and the power-law decay of J_c [$J_c \sim H^{-\alpha}(\alpha \sim 0.5)$] at the low-field region, which are attributed to the strong pinning contribution [27,28].

On the other hand, it has been also shown that the overall pinning properties of Fe-based superconductors have been successfully explained in terms of collective pinning and vortex creep [29–34,45,73]. Based on these considerations, in this section we apply the collective pinning and creep model to our results and extract the trend in the doping-dependent J_c. It is pointed out that the strong pinning contribution rapidly decreases in $H(J_c \sim H^{-\alpha})$ and the weak collective pinning contribution becomes dominant with increasing H ($>$ 0.1–1 T), therefore, one can approximate the T dependence of J_c at high H by collective pinning contributions.

At around zero field and at higher fields, J_c is dominated by the self-field effect [74,75] and the SMP effect, respectively, which hinders a meaningful application of collective pinning theory in these regions. On the other hand, collective pinning theory is applicable in the moderate-H regions, when thermally activated flux motion and collective pinning/creep [76] are to be taken into account. Two types of pinning mechanisms, namely, δT_c pinning caused by the spatial variation of T_c and δl pinning caused by the fluctuation in the mean free path (l) [42], have to be considered. The corresponding T dependence of J_c is then described by the following formula [44,77], using the reduced temperature $t = T/T_c$:

$$J_c(t) = J_{c0}J(t)/[1 + \mu k_B T C/U_0 g(t)]^{1/\mu},$$

where J_{c0} is J_c at $T = 0$ K, μ is the glassy exponent characterizing the vortex creep regime (single vortex, small bundle, etc.), k_B is the Boltzmann constant, U_0 is the pinning potential, and C is a constant related to the hopping attempt frequency. For $H < H_{on}$, it is known that μ can be treated as a constant [30,78]. Assuming the single-vortex pinning, the T-dependent terms $J(t)$ and $g(t)$ are expressed as [79]

$$J(t) = (1-t^2)^{7/6}(1 + t^2)^{5/6},$$

$$g(t) = (1-t^2)^{1/3}(1 + t^2)^{5/3}$$

for δT_c pinning and

$$J(t) = (1-t^2)^{5/2}(1 + t^2)^{-1/2}, \quad g(t) = 1-t^4$$

for δl pinning. Based on the collective pinning model [42], the condition that the above formulas are applicable is $H < B_{SB} \sim 5(J_c/J_d)H_{c2}$, where J_d is the depairing current. In the case of K-Ba122 ($x = 0.30$), B_{SB} is estimated as $\sim$1.5 T using $J_c \sim 6 \times 10^5$ A/cm^2, $J_d \sim 2 \times 10^8$ A/cm^2 [80], and $\mu_0 H_{c2} \sim$ 100 T. Similarly, B_{SB} is ~ 1.6 T for Co-Ba122 ($x = 0.06$) and $\sim$1.4 T for P-Ba122 ($x = 0.30$). For the present analysis, $J_c(T)$ at $\mu_0 H = 0.4$ T are employed.

The $J_c(t)$ caused by δT_c pinning [$J_c^{\delta T_c}(T)$] and $J_c(t)$ caused by δl pinning [$J_c^{\delta l}(T)$] exhibit different T dependences. In particular, at intermediate T, $J_c^{\delta l}(T)$ decreases much faster than $J_c^{\delta T_c}(T)$. In order to extract the contributions of the two pinning mechanisms, we fitted the experimental results using a function $J_c(T) = J_c^{\delta T_c}(T) + J_c^{\delta l}(T)$. It should be noted that the formula is not exact since the sum of the two contributions is not necessarily additive. Nevertheless, as shown below, this simple formula successfully picks up the dominant pinning mechanism, particularly when one overwhelms the other, as well as the doping evolution of the two contributions. To fit data, we used four parameters: μ, $k_B C/U_0$ (K^{-1}),

$J_{c0}^{\delta T_c}$ [$= J_c^{\delta T_c}(0)$] (MA/cm^2), and $J_{c0}^{\delta l}$ [$= J_c^{\delta l}(0)$] (MA/cm^2). For μ and $k_B C/U_0$, we took the reported values obtained from the magnetization-relaxation measurements [30,78]. Note that we employed the same μ and $k_B C/U_0$ for $J_c^{\delta T_c}(T)$ and $J_c^{\delta l}(T)$, which are not necessarily the same for different pinning mechanisms. This is because, when one mechanism is dominant, $J_c(T)$ is mostly described by either $J_c^{\delta T_c}(T)$ or $J_c^{\delta l}(T)$, therefore the values of μ and C/U_0 represent the dominant mechanism and the minor contribution does not affect the results. Indeed, as shown in the Appendix, the main results do not depend on the magnitude of these parameters.

Figures 12(a)–12(d) show $J_c(T)$ for K-Ba122 plotted on a semilogarithmic scale. Here black circles are experimental results. Dashed curves are the results obtained through the fitting. The blue dashed and red dashed curves are the contributions from the δT_c pinning and the δl pinning, respectively, and the black dashed curves are their sums. For $x = 0.23$, the δl pinning is larger than the δT_c pinning at low T. With increasing T, the δT_c pinning increases and becomes dominant at $T > 10$ K.

In the case of $x = 0.30$ [Fig. 12(b)], which possesses the highest J_c among K-Ba122, $J_c(T)$ decreases linearly over a wide T range between 5 and 20 K, followed by a steeper falloff at higher T. This is the typical behavior of δl pinning. Indeed, $J_c(T)$ is fitted well by δl pinning alone up to 20 K, with a significant contribution from δT_c pinning only close to T_c. The fitting parameters μ, $k_B C/U_0$, and $J_{c0}^{\delta T_c}$ are the same as those used for $x = 0.23$, whereas $J_{c0}^{\delta l}$ is larger by one order of magnitude.

Figure 12(c) shows $J_c(T)$ for $x = 0.33$. The overall T dependence is similar to that for $x = 0.23$, rather than for $x = 0.30$, in the sense that it shows a concave T dependence with a hump at $T \sim 25$ K. The hump feature is characteristic of δT_c pinning. The fitting result shows that the δl pinning contributes the most below 15 K, while δT_c pinning becomes dominant at higher T. In this case, a small-μ value reproduces the experimental results, which indicates a faster flux creep. For $x = 0.51$, $J_c(T)$ is reproduced well by δT_c pinning alone and the contribution from the δl pinning is smaller by more than one order of magnitude even at the lowest T.

The obtained results indicate that the dominant pinning mechanism of K-Ba122 changes depending on T and x. To see the x dependences of the two pinning contributions, $J_c^{\delta T_c}$ and $J_c^{\delta l}$ at $T = 0.3T_c$ are plotted in Fig. 13(a). The contribution from δT_c pinning (blue circles) shows a modest x dependence, with a maximum at $x = 0.25$. On the other hand, the contribution from the δl pinning exhibits a pronounced peak at $x = 0.30$. The present analysis suggests that the strong enhancement in J_c for $x = 0.30$ is mainly due to strong δl pinning, which is special to this composition.

Figures 12(e)–12(h) show $J_c(T)$ for Co-Ba122. For $x = 0.05$, shown in Fig. 12(e), the δT_c pinning is dominant for the entire T range, while δl pinning makes certain contributions at low T, up to one-third of the total J_c. Figure 12(f) shows $J_c(T)$ for $x = 0.057$, which possesses the highest J_c for Co-Ba122. Here the experimental data exhibit a convex T dependence. This behavior resembles K-Ba122 with $x = 0.30$ and indicates that δl pinning plays a dominant role, although the contribution from δT_c pinning is pronounced near T_c. For
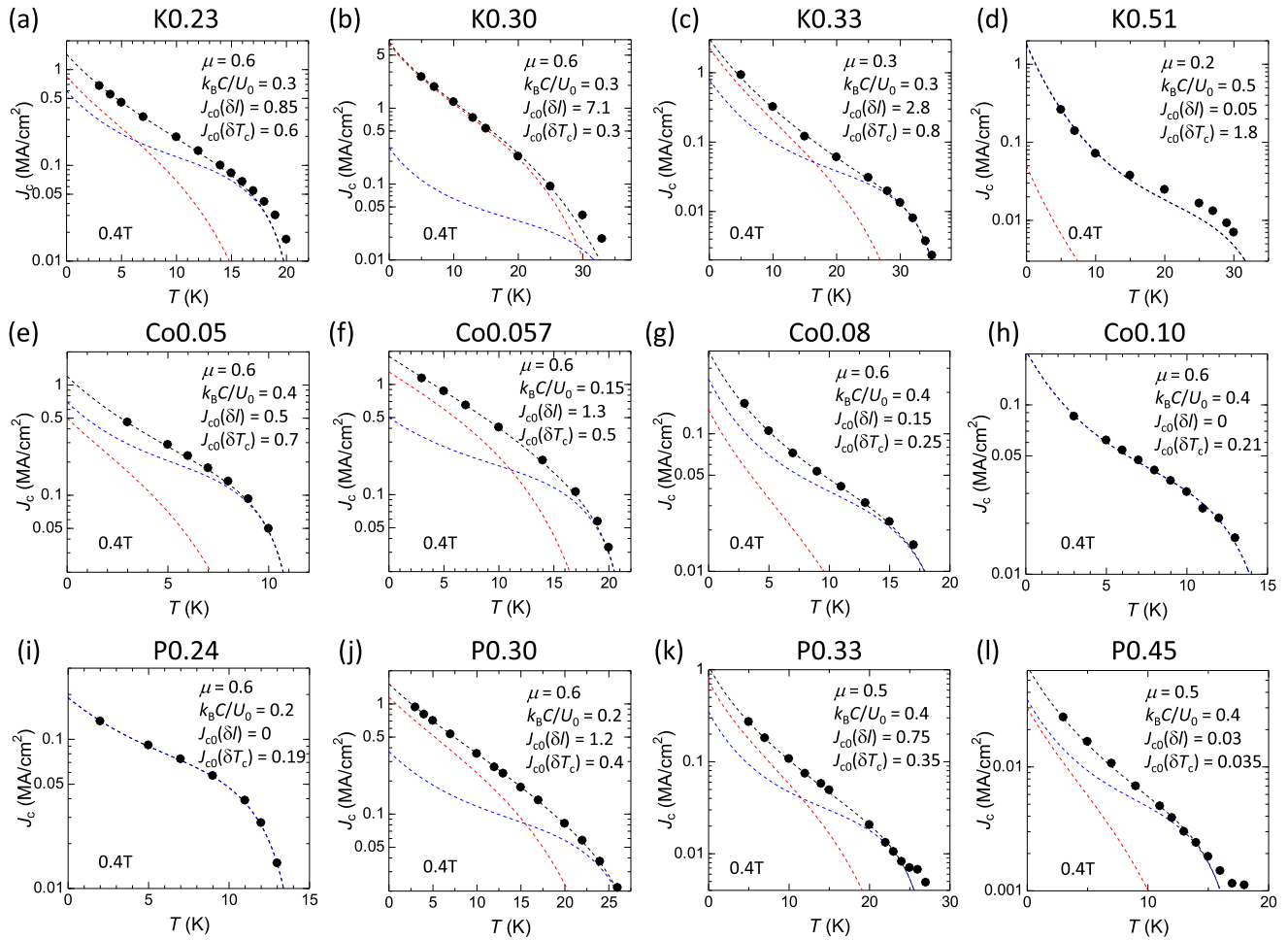
FIG. 12. Temperature dependence of J_c for selected compounds: (a)–(d) $Ba_{1-x}K_xFe_2As_2$ ($x = 0.23, 0.30, 0.33$, and 0.51), (e)–(h) $Ba(Fe_{1-x}Co_x)_2As_2$ ($x = 0.05, 0.057, 0.08$, and 0.10), and (i)–(l) $BaFe_2(As_{1-x}P_x)_2$ ($x = 0.24, 0.30, 0.33$, and 0.45). The black, blue, and red dashed curves indicate the total J_c, δT_c pinning, and δl pinning components, respectively. The parameters used for the fitting are shown in each panel (units for k_BC/U_0 and J_{c0} are K^{-1} and MA/cm^2, respectively).

the overdoped sample with $x = 0.08$ shown in Fig. 12(g), $J_c(T)$ shows a concave T dependence at ~ 8 K, which is characteristic for δT_c pinning. The result indicates that the δl pinning significantly weakens between $x = 0.057$ and 0.08. For $x = 0.10$ [Fig. 12(h)], $J_c(T)$ is reasonably fitted by the δT_c pinning contribution alone. In Fig. 13(b), the x dependence of $J_c^{\delta T_c}$ and $J_c^{\delta l}$ of Co-Ba122 at $T = 0.3T_c$ is plotted. As in the case of K-Ba122, the δT_c pinning is enhanced in the underdoped region and the δl pinning shows a sharp peak at $x \sim 0.06$. It is also noted that the contribution from δT_c pinning is larger for Co-Ba122 compared to K-Ba122.

Figures 12(e)–12(h) show $J_c(T)$ for P-Ba122. For $x = 0.24$ [Fig. 12(i)], the experimental data are well reproduced by δT_c pinning alone. On the other hand, for $x = 0.30$, which possesses the highest J_c for P-Ba122, $J_c(T)$ shows a linear T dependence between 5 and 15 K and the slope becomes steeper at higher temperatures, which is the characteristic of δl pinning, similar to the high-J_c K- and Co-Ba122 samples [Figs. 12(b) and 12(f)]. The fitting result indeed shows that δl pinning is dominant at low T, while δT_c pinning is pronounced near T_c. The $J_c(T)$ curve of the slightly overdoped sample with $x = 0.33$ [Fig. 12(k)] can be expressed as a sum of

the δT_c pinning and the δl pinning contributions with a ratio similar to that for $x = 0.30$. The result indicates that both contributions are equally suppressed from $x = 0.30$ to $x = 0.33$. For $x = 0.45$ [Fig. 12(l)], the magnitude of the two contributions decrease by one order of magnitude compared with $x = 0.33$. Here the δT_c pinning contribution is larger for the whole temperature range. Figure 13(c) depicts the x dependence of $J_c^{\delta T_c}$ and $J_c^{\delta l}$ of P-Ba122 at $T = 0.3T_c$. In this case, both δT_c pinning and δl pinning components show a peak at $x = 0.30$.

To summarize, common to the three cases, a significant enhancement of the δl pinning is observed for high-J_c samples, particularly at low T. Also, the δT_c pinning, which becomes important at high T, tends to be enhanced on the underdoped side. Both contributions significantly decrease on the overdoped side.

Note that the present fitting based on the collective pinning model may not be adequate for several samples. Also, $J_c(T)$ data at high T tend to be affected by the SMP, which shifts to lower H with increasing T, leading to the overestimation of the δT_c pinning. However, this does not affect our conclusion because (1) J_c of those cases is one order of magnitude smaller
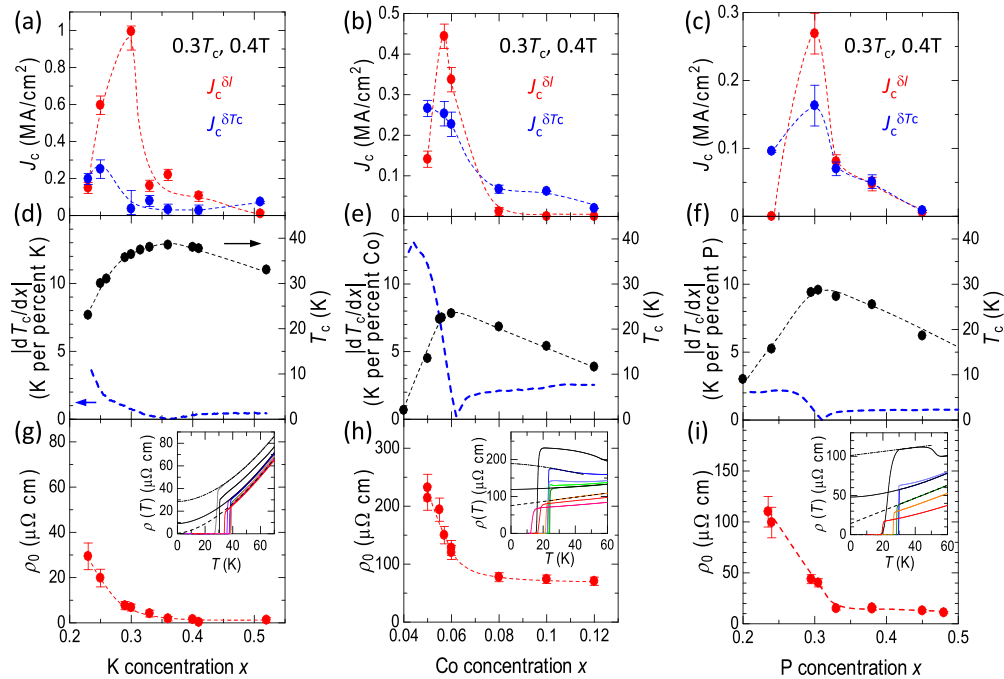
FIG. 13. (a)–(c) Doping dependence of $J_c^{\delta T_c}$ and $J_c^{\delta l}$ at $\mu_0 H = 0.4$ T and $T = 0.3T_c$, (d)–(f) T_c and magnitude of dT_c/dx, and (g)–(i) residual resistivity extracted from power-law fitting (several examples are shown in the inset) for K-Ba122 (left), Co-Ba122 (middle), and P-Ba122 (right), respectively. The dashed lines are guides for the eye.

than for the high-J_c samples and (2) we found a significant enhancement of δl pinning to be responsible for high J_c.

C. Possible sources for δT_c pinning and δl pinning

In this section we discuss the possible sources for δT_c and δl pinning. By definition, δT_c pinning is caused by the spatial variation in T_c. In the Ba122 system, T_c is determined by the concentration of dopant atoms, i.e., x. In such a situation, the spatial variation in T_c (ΔT_c) is introduced by the spatial inhomogeneity of the dopant atom distribution and is expressed as

$$\Delta T_c = |dT_c/dx|\Delta x,$$

where dT_c/dx is the slope of the $T_c(x)$ curve and Δx is its spatial variation in x. The formula implies that ΔT_c becomes large if T_c strongly depends on x (dT_c/dx is large). On the other hand, the δl pinning is associated with the spatial variation of the mean free path l of the charge carriers. Experimentally, l is related to the resistivity $\rho(T)$ by the formula

$$\rho(\mathrm{T}) = (\hbar/e^2)\left(3\pi^2/n_0^2\right)^{1/3}/l,$$

where n_0 is the carrier density. In particular, the residual resistivity ρ_0, the T-independent part of the normal state resistivity, directly reflects l associated with the spatial inhomogeneity.

The x dependence of $J_c^{\delta T_c}$ and $J_c^{\delta l}$ for K-, Co-, and P-Ba122 are shown in Figs. 13(a)–13(c). In Figs. 13(d)–13(f) we show the x dependence of $|dT_c/dx|$ (blue dashed line) derived from the $T_c(x)$ curve (black dashed line); $|dT_c/dx|$ becomes zero at $T_c^{\max}$ and $x = 0.36$ for K-Ba122, $x = 0.06$ for Co-Ba122, and $x = 0.31$ for P-Ba122. In all cases, the $T_c(x)$ curve is more inclined on the underdoped side compared with the overdoped side. As a result, $|dT_c/dx|$ is always larger on the underdoped

side. This tendency is consistent with enhanced δT_c pinning in the underdoped region as seen in Figs. 13(a)–13(c). Moreover, $|dT_c/dx|$ of Co-Ba122 is larger than for K- and P-Ba122 and persists up to the overdoped region, which likely enhances the δT_c pinning in Co-Ba122. Assuming the local variation in T_c caused by the inhomogeneous distribution of dopant elements, the doping and dopant dependence of the δT_c pinning can be well explained.

Next we discuss the possible relationship between ρ_0 and the δl pinning. In Figs. 13(g)–13(i) we show the x dependence of ρ_0 in K-, Co-, and P-Ba122. Here ρ_0 is estimated by fitting $\rho_{ab}(T)$ using the formula $\rho_{ab}(T) = \rho_0 + AT^n$ at low T, typically below 80 K. Examples of the fitting results are shown in the insets. For all the cases, ρ_0 is large in the underdoped samples and rapidly decreases with x toward the optimally doped region. In the overdoped region, ρ_0 does not depend on x. In the optimally and the overdoped region, there is a correlation between ρ_0 and $J_c^{\delta l}$, namely, both quantities are small in the overdoped region, and towards the optimally doped region, they sharply increase at the same x. In the heavily underdoped region, the two quantities exhibit different x dependences. With decreasing x, $J_c^{\delta l}$ begins to decrease, whereas ρ_0 continues to increase. It may be because of the weakening of the pinning energy due to the decrease in condensation energy.

The reason for the enhanced ρ_0 in the underdoped region is not clear at the moment. Impurity scattering from the dopant atoms themselves may not be the origin, because ρ_0 decreases with an increasing number of dopant atoms. This tendency is opposite to what we expect from the impurity scattering. Furthermore, K atoms are located away from the FeAs planes and thus should not be effective scattering centers compared with Co atoms, which directly substitute

for Fe atoms. This contradicts the fact that ρ_0 of underdoped K-Ba122 is comparable to those for Co- and P-Ba122. One possible scenario is that in the heavily underdoped region, the AFO phase coexists with the SC phase in a microscopic length scale as has been suggested by muon spin rotation, nuclear magnetic resonance, etc. [81–83]. In such a situation, the material become microscopically inhomogeneous, which results in limiting l. The δT_c pinning is also expected to increase, since the AFO phase is a non-SC and thus works as δT_c disorder.

There are several proposals that highlight the AFO-PT phase transitions. Based on the noticeable enhancement in J_c in slightly underdoped Co-Ba122, Prozorov *et al.* proposed that the twin domain boundaries of the orthorhombic phase act as pinning centers [40]. Later, Kalisky *et al.* carried out the scanning superconducting quantum interference device susceptometry on Co-Ba122 and reported that the superfluid density is enhanced on the twin boundaries [84]. The authors suggest that the enhancement in the superfluid density at the twin boundary results in an enhanced J_c [85]. The phase diagrams of the K-Ba122 [Fig. 1(i)], Co-Ba122 [Fig. 4(i)], and P-Ba122 [Fig. 7(i)] obtained in the present study are compatible with these proposals, in that the highest-J_c compositions nearly coincide with the critical concentration for the AFO transition in all three cases. It is also likely that the twin domain boundary acts as a scattering center and causes the δl pinning. Likewise, an inhomogeneous superfluid density produces the δT_c pinning. Measurements on the detwinned single crystals would answer the question whether the twin domain boundary is indeed responsible for the enhanced J_c.

The above arguments are more or less based on the conventional viewpoints. A more exotic scenario that is related to quantum criticality has been proposed by Putzke *et al.* [86] Based on the detailed upper- and lower-critical-field measurements on P-Ba122, they proposed that the energy of superconducting vortices is enhanced near the possible quantum critical point (QCP) at $x \sim 0.3$, possibly due to a microscopic mixing of antiferromagnetism and superconductivity. Based on the scenario, the vortex state of the Fe-based superconductors is highly unusual. Their results are apparently consistent with the spikelike enhancement in J_c observed in the present study. On the other hand, if the scenario is correct, one would naturally expect that the QCP also exists in K-Ba122 and Co-Ba122. We are unaware of any confirming experimental evidence that supports the QCP in these materials.

Toward applications, the present results suggest that the introduction of δl pinning disorder is an effective way to enhance J_c. It may be possible that the introduction of the δl pinning into the highest-T_c sample results in a material possessing both the highest T_c and the highest J_c. In this regard, codoping of Co into optimally doped K-Ba122 would be intriguing.

Finally, we briefly compare the present results with another candidate for applications, i.e., the 1111 system, which possesses the highest $T_c^{\max} \sim 56$ K and a relatively large anisotropy $\gamma \sim 5$–10. Reflecting the larger γ, a significant broadening of resistive transition under H is observed in 1111 system [87]. The reported $J_c \sim 2$ MA/cm^2 at 5 K and 0 T in SmFeAsO$_{0.7}$F$_{0.25}$ ($T_c \sim 50$ K) [11] is comparable with that of K-Ba122, while T_c is higher by $\sim$12 K, suggestive of a

weaker pinning. Indeed, it is reported that the vortex dynamics in the 1111 system is governed by a Josephson-like vortex behavior at low T, leading to a weak interaction between vortices and pinning sites [88]. These features indicate that the nature of pinning in the 1111 system is different from that in the 122 system. At the moment, the doping dependence of J_c in the 1111 system is unclear. It is expected that the doping dependence of J_c is different from that in the 122 system owing to the larger anisotropy and the consequent difference in nature of pinning. On the other hand, because the electronic phase diagram of the 1111 system is more or less similar to that of the 122 system, a larger J_c may be achieved through the optimization of the doping level, presumably around a slightly underdoped region, as demonstrated in this work.

V. CONCLUSION

In this study we studied the dependence of J_c for K-, Co-, and P-Ba122 on the dopant concentration using high-quality single crystals and established the doping dependence of J_c. The J_c showed a variety of H and T dependences depending on the variation and concentration of dopant elements. On the other hand, in all the cases, the magnitude of J_c was sharply enhanced at doping levels corresponding to the slightly underdoped to optimally doped region. The common enhancement of J_c in spite of the distinct character (charge type and the substitution site) of dopants indicates that the behavior comes from an intrinsic origin, which is likely related to the underlying electronic phase diagram. The analysis of $f_p(h)$ showed a similar $h_{\max}$ value for high-J_c samples, suggesting that a common pinning mechanism is responsible for enhancing J_c. Based on the T dependence of J_c, it was found that both the δT_c pinning and the δl pinning are enhanced in the underdoped region. The extracted results are consistent with the larger $|dT_c/dx|$ as well as the increase of ρ_0 on the underdoped side, which indicates enhanced δT_c and δl disorder, respectively.

APPENDIX: FITTING-PARAMETER DEPENDENCE OF δT_c AND δl PINNING CONTRIBUTIONS

In Fig. 12 in we showed the results of fitting our data by using the parameters shown in each panel. Because we did not obtain μ and C/U_0 experimentally, these parameters can be arbitrarily chosen, although we referred to reported values. In fact, one can fit the data by using different parameter sets, possibly resulting in a considerable uncertainty arising from
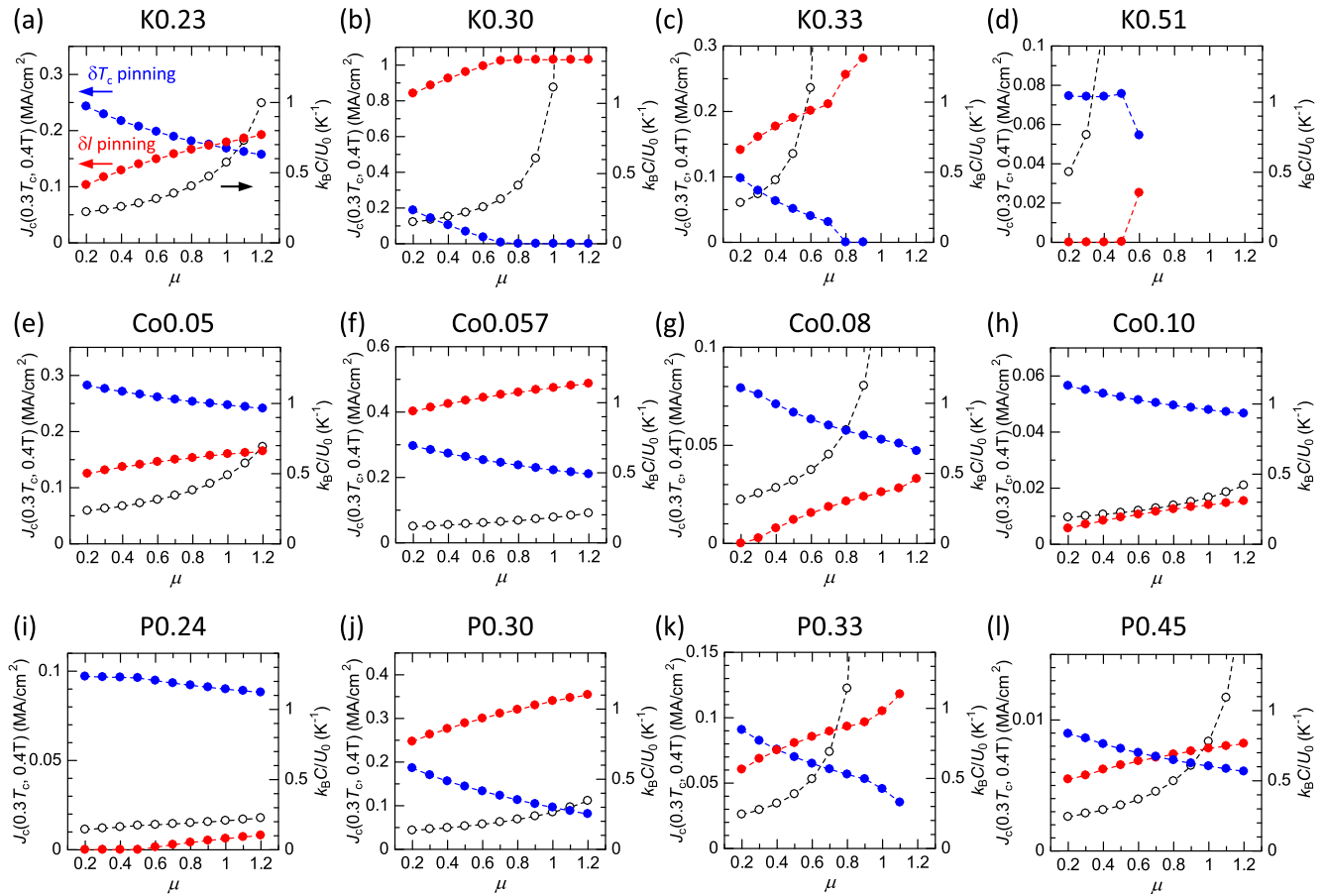
FIG. 14. Dependence of the δT_c pinning (blue circles) and δl pinning (red circles) contributions on μ for the representative samples corresponding to Fig. 12. The derived $k_B C/U_0$ values are also plotted (black open circles).

the choice of these parameters. In order to check how much the results depend on the choice of the parameters, we varied μ in the range of 0.2–1.2 (which covers the reported values for iron pnictides) and carried out the fitting. Figures 14(a)–14(l) show the μ dependence of the δT_c and δl pinning contributions (the derived $k_B C/U_0$ values are also plotted). The samples correspond to those used in Fig. 12. In most cases, the dominant contribution does not change for any μ values.

For several samples [Figs. 14(a), 14(k), and 14(l)], where the contributions from δT_c and δl pinning are comparable, the dominant contribution changes when μ is varied, although they are still comparable to each other. The results show that the overall doping dependence of δT_c and δl pinning contributions is robust against the choice of μ, hence it does not change our conclusion. The error bars in Figs. 13(a)–13(c) indicate the uncertainty arising from the μ dependence.

[1] M. Putti *et al.*, Supercond. Sci. Technol. **23**, 034003 (2010).

[2] J. Shimoyama, Supercond. Sci. Technol. **27**, 044002 (2014).

[3] H. Hosono, K. Tanabe, E. Takayama-Muromachi, H. Kageyama, S. Yamanaka, H. Kumakura, M. Nohara, H. Hiramatsu, and S. Fujitsu, Sci. Technol. Adv. Mater. **16**, 033503 (2015).

[4] X. Zhang, C. Yao, H. Lin, Y. Cai, Z. Chen, J. Li, C. Dong, Q. Zhang, D. Wang, Y. Ma, H. Oguro, S. Awaji, and K. Watanabe, Appl. Phys. Lett. **104**, 202601 (2014).

[5] Z. Gao, K. Togano, A. Matsumoto, and H. Kumakura, Supercond. Sci. Technol. **28**, 012001 (2015).

[6] A. Matsumoto, Z. Gao, K. Togano, and H. Kumakura, Supercond. Sci. Technol. **27**, 025011 (2014).

[7] H. Sato, H. Hiramatsu, T. Kamiya, and H. Hosono, Appl. Phys. Lett. **104**, 182603 (2014).

[8] T. Katase, Y. Ishimaru, A. Tsukamoto, H. Hiramatsu, T. Kamiya, K. Tanabe, and H. Hosono, Nat. Commun. **2**, 409 (2011).

[9] Y. Nakajima, Y. Tsuchiya, T. Taen, T. Tamegai, S. Okayasu, and M. Sasase, Phys. Rev. B **80**, 012510 (2009).

[10] L. Fang, Y. Jia, C. Chaparro, G. Sheet, H. Claus, M. A. Kirk, A. E. Koshelev, U. Welp, G. W. Crabtree, W. K. Kwok, S. Zhu, H. F. Hu, J. M. Zuo, H.-H. Wen, and B. Shen, Appl. Phys. Lett. **101**, 012601 (2012).

[11] L. Fang, Y. Jia, V. Mishra, C. Chaparro, V. K. Vlasko-Vlasov, A. E. Koshelev, U. Welp, G. W. Crabtree, S. Zhu, N. D. Zhigadlo, S. Katrych, J. Karpinski, and W. K. Kwok, Nat. Commun. **4**, 2655 (2013).

[12] C. J. van der Beek, S. Demirdiş, D. Colson, F. Rullier-Albenque, Y. Fasano, T. Shibauchi, Y. Matsuda, S. Kasahara, P. Gierlowski, and M. Konczykowski, J. Phys.: Conf. Ser. **449**, 012023 (2013).

[13] J. H. Durrell, C.-B. Eom, A. Gurevich, E. E. Hellstrom, C. Tarantini, A. Yamamoto, and D. C. Larbalestier, Rep. Prog. Phys. **74**, 124511 (2011).

[14] Y.-J. Kim, J. D. Weiss, E. E. Hellstrom, D. C. Larbalestier, and D. N. Seidman, Appl. Phys. Lett. **105**, 162604 (2014).

[15] M. V. Feigel'man, V. B. Geshkenbein, A. I. Larkin, and V. M. Vinokur, Phys. Rev. Lett. **63**, 2303 (1989).

[16] M. V. Feigel'man, V. B. Geshkenbein, A. I. Larkin, Physica C **167**, 177 (1990).

[17] V. M. Vinokur, P. H. Kes, and A.E. Koshelev, Physica C **168**, 29 (1990).

[18] M. P. A. Fisher, Phys. Rev. Lett. **62**, 1415 (1989).

[19] P. L. Gammel, L. F. Schneemeyer, J. V. Waszczak, and D. J. Bishop, Phys. Rev. Lett. **61**, 1666 (1988).

[20] D. Ertas and D. R. Nelson, Physica C **272**, 79 (1996).

[21] T. Giamarchi and P. Le Doussal, Phys. Rev. B **55**, 6577 (1997).

[22] V. Vinokur, B. Khaykovich, E. Zeldov, M. Konczykowski, R. A. Doyle, and P. Kes, Physica C **295**, 209 (1998).

[23] B. Rosenstein and A. Knigavko, Phys. Rev. Lett. **83**, 844 (1999).

[24] H. Yang, H. Luo, Z. Wang, and H.-H. Wen, Appl. Phys. Lett. **93**, 142506 (2008).

[25] A. K. Pramanik, L. Harnagea, C. Nacke, A. U. B. Wolter, S. Wurmehl, V. Kataev, and B. Büchner, Phys. Rev. B **83**, 094502 (2011).

[26] T. Taen, Y. Tsuchiya, Y. Nakajima, and T. Tamegai, Phys. Rev. B **80**, 092502 (2009).

[27] C. J. van der Beek, G. Rizza, M. Konczykowski, P. Fertey, I. Monnet, Thierry Klein, R. Okazaki, M. Ishikado, H. Kito, A. Iyo, H. Eisaki, S. Shamoto, M. E. Tillman, S. L. Bud'ko, P. C. Canfield, T. Shibauchi, and Y. Matsuda, Phys. Rev. B **81**, 174517 (2010).

[28] C. J. van der Beek, M. Konczykowski, S. Kasahara, T. Terashima, R. Okazaki, T. Shibauchi, and Y. Matsuda, Phys. Rev. Lett. **105**, 267002 (2010).

[29] R. Prozorov, N. Ni, M. A. Tanatar, V. G. Kogan, R. T. Gordon, C. Martin, E. C. Blomberg, P. Prommapan, J. Q. Yan, S. L. Bud'ko, and P. C. Canfield, Phys. Rev. B **78**, 224506 (2008).

[30] B. Shen, P. Cheng, Z. Wang, L. Fang, C. Ren, L. Shan, and H.-H. Wen, Phys. Rev. B **81**, 014503 (2010).

[31] S. Salem-Sugui, Jr., L. Ghivelder, A. D. Alvarenga, L. F. Cohen, K. A. Yates, K. Morrison, J. L. Pimentel, Jr., H. Luo, Z. Wang, and H.-H. Wen, Phys. Rev. B **82**, 054513 (2010).

[32] T. Taen, Y. Tsuchiya, Y. Nakajima, and T. Tamegai, Physica C **470**, 1106 (2010).

[33] Y. Sun, T. Taen, Y. Tsuchiya, S. Pyon, Z. Shi, and T. Tamegai, Europhys. Lett. **103**, 57013 (2013).

[34] W. Zhou, X. Xing, W. Wu, H. Zhao, and Z. Shi, Sci. Rep. **6**, 22278 (2016).

[35] P. Das, A. D. Thakur, A. K. Yadav, C. V. Tomy, M. R. Lees, G. Balakrishnan, S. Ramakrishnan, and A. K. Grover, Phys. Rev. B **84**, 214526 (2011).

[36] D. Miu, T. Noji, T. Adachi, Y. Koike, and L. Miu, Supercond. Sci. Technol. **25**, 115009 (2012).

[37] R. Kopeliansky, A. Shaulov, B. Y. Shapiro, Y. Yeshurun, B. Rosenstein, J. J. Tu, L. J. Li, G. H. Cao, and Z. A. Xu, Phys. Rev. B **81**, 092504 (2010).

[38] S. Salem-Sugui, Jr., L. Ghivelder, A. D. Alvarenga, L. F. Cohen, H. Luo, and X. Lu, Phys. Rev. B **84**, 052510 (2011).

[39] A. Yamamoto, J. Jaroszynski, C. Tarantini, L. Balicas, J. Jiang, A. Gurevich, D. C. Larbalestier, R. Jin, A. S. Sefat, M. A. McGuire, B. C. Sales, D. K. Christen, and D. Mandrus, Appl. Phys. Lett. **94**, 062511 (2009).

[40] R. Prozorov, M. A. Tanatar, N. Ni, A. Kreyssig, S. Nandi, S. L. Bud'ko, A. I. Goldman, and P. C. Canfield, Phys. Rev. B **80**, 174517 (2009).

[41] D. L. Sun, Y. Liu, and C. T. Lin, Phys. Rev. B **80**, 144515 (2009).

[42] G. Blatter, M. V. Feigel'man, V. B. Geshkenbein, A. I. Larkin, and V. M. Vinokur, Rev. Mod. Phys. **66**, 1125 (1994).

[43] M. Shahbazi, X. L. Wang, K. Y. Choi, and S. X. Dou, Appl. Phys. Lett. **103**, 032605 (2013).

[44] S. R. Ghorbani, X. L. Wang, M. Shahbazi, S. X. Dou, and C. T. Lin, Appl. Phys. Lett. **100**, 212601 (2012).

[45] T. Taen, Y. Nakajima, T. Tamegai, and H. Kitamura, Phys. Rev. B **86**, 094527 (2012).

[46] D. Song, S. Ishida, A. Iyo, M. Nakajima, J. Shimoyama, M. Eisterer, and H. Eisaki, Sci. Rep. **6**, 26671 (2016).

[47] S. Demirdiş, Y. Fasano, S. Kasahara, T. Terashima, T. Shibauchi, Y. Matsuda, M. Konczykowski, H. Pastoriza, and C. J. van der Beek, Phys. Rev. B **87**, 094506 (2013).

[48] K. Kihou, T. Saito, K. Fujita, S. Ishida, M. Nakajima, K. Horigane, H. Fukazawa, Y. Kohori, S. Uchida, J. Akimitsu, A. Iyo, C. H. Lee, and H. Eisaki, J. Phys. Soc. Jpn. **85**, 034718 (2016).

[49] M. Nakajima, S. Ishida, K. Kihou, Y. Tomioka, T. Ito, Y. Yoshida, C. H. Lee, H. Kito, A. Iyo, H. Eisaki, K. M. Kojima, and S. Uchida, Phys. Rev. B **81**, 104528 (2010).

[50] M. Nakajima, S. Uchida, K. Kihou, C. H. Lee, A. Iyo, and H. Eisaki, J. Phys. Soc. Jpn. **81**, 104710 (2012).

[51] C. P. Bean, Rev. Mod. Phys. **36**, 31 (1964).

[52] B. Shen, H. Yang, Z.-S. Wang, F. Han, B. Zeng, L. Shan, C. Ren, and H.-H. Wen, Phys. Rev. B **84**, 184512 (2011).

[53] N. R. Werthamer, E. Helfand, and P. C. Hohenberg, Phys. Rev. **147**, 295 (1966).

[54] Y. Liu, M. A. Tanatar, W. E. Straszheim, B. Jensen, K. W. Dennis, R. W. McCallum, V. G. Kogan, R. Prozorov, and T. A. Lograsso, Phys. Rev. B **89**, 134504 (2014).

[55] H.-J. Kim, Y. Liu, Y. S. Oh, S. Khim, I. Kim, G. R. Stewart, and K. H. Kim, Phys. Rev. B **79**, 014514 (2009).

[56] T. Taen, F. Ohtake, S. Pyon, T. Tamegai, and H. Kitamura, Supercond. Sci. Technol. **28**, 085003 (2015).

[57] B. Rosenstein, B. Y. Shapiro, I. Shapiro, Y. Bruckental, A. Shaulov, and Y. Yeshurun, Phys. Rev. B **72**, 144512 (2005).

[58] G. P. Mikitik and E. H. Brandt, Phys. Rev. B **64**, 184514 (2001).

[59] N. Ni, M. E. Tillman, J.-Q. Yan, A. Kracher, S. T. Hannahs, S. L. Bud'ko, and P. C. Canfield, Phys. Rev. B **78**, 214515 (2008).

[60] J.-H. Chu, J. G. Analytis, C. Kucharczyk, and I. R. Fisher, Phys. Rev. B **79**, 014506 (2009).

[61] S. Kasahara, T. Shibauchi, K. Hashimoto, K. Ikada, S. Tonegawa, R. Okazaki, H. Shishido, H. Ikeda, H. Takeya, K. Hirata, T. Terashima, and Y. Matsuda, Phys. Rev. B **81**, 184519 (2010).

[62] J. G. Analytis, H.-H. Kuo, R. D. McDonald, M. Wartenbe, P. M. C. Rourke, N. E. Hussey, and I. R. Fisher, Nat. Phys. **10**, 194 (2014).

[63] R. Meier-Hirmer, H. Küpfer, and H. Scheurer, Phys. Rev. B **31**, 183 (1985).

[64] C. A. M. van der Klein, P. H. Kes, and D. de Klerk, Philos. Mag. **29**, 559 (1974).

[65] M. Zehetmayer, M. Eisterer, J. Jun, S. M. Kazakov, J. Karpinski, B. Birajdar, O. Eibl, and H. W. Weber, Phys. Rev. B **69**, 054510 (2004).

[66] M. Zehetmayer, M. Eisterer, C. Krutzler, J. Jun, S. M. Kazakov, J. Karpinski, and H. W. Weber, Supercond. Sci. Technol. **20**, S247 (2007).

[67] S. Salem-Sugui, Jr., J. Mosqueira, A. D. Alvarenga, D. Sóñora, E. P. Herculano, D. Hu, G. Chen, and H. Luo, Supercond. Sci. Technol. **28**, 055017 (2015).

[68] L. Fang, Y. Jia, J. A. Schlueter, A. Kayani, Z. L. Xiao, H. Claus, U. Welp, A. E. Koshelev, G. W. Crabtree, and W.-K. Kwok, Phys. Rev. B **84**, 140504(R) (2011).

[69] D. Dew-Hughes, Philos. Mag. **30**, 293 (1974).

[70] D. S. Inosov, T. Shapoval, V. Neu, U. Wolff, J. S. White, S. Haindl, J. T. Park, D. L. Sun, C. T. Lin, E. M. Forgan, M. S. Viazovska, J. H. Kim, M. Laver, K. Nenkov, O. Khvostikova, S. Kühnemann, and V. Hinkov, Phys. Rev. B **81**, 014513 (2010).

[71] M. R. Eskildsen, L. Y. Vinnikov, T. D. Blasius, I. S. Veshchunov, T. M. Artemova, J. M. Densmore, C. D. Dewhurst, N. Ni, A. Kreyssig, S. L. Bud'ko, P. C. Canfield, and A. I. Goldman, Phys. Rev. B **79**, 100501(R) (2009).

[72] Y. Yin, M. Zech, T. L. Williams, X. F. Wang, G. Wu, X. H. Chen, and J. E. Hoffman, Phys. Rev. Lett. **102**, 097002 (2009).

[73] M. Bonura, E. Giannini, R. Viennois, and C. Senatore, Phys. Rev. B **85**, 134532 (2012).

[74] M. Däumling and D. C. Larbalestier, Phys. Rev. B **40**, 9350(R) (1989).

[75] E. Zeldov, A. I. Larkin, V. B. Geshkenbein, M. Konczykowski, D. Majer, B. Khaykovich, V. M. Vinokur, and H. Shtrikman, Phys. Rev. Lett. **73**, 1428 (1994).

[76] J. R. Thompson, Y. R. Sun, L. Civale, A. P. Malozemoff, M. W. McElfresh, A. D. Marwick, and F. Holtzberg, Phys. Rev. B **47**, 14440 (1993).

[77] H.-H. Wen, Z. X. Zhao, Y. G. Xiao, B. Yin, and J. W. Li, Physica C **251**, 371 (1995).

[78] M. Konczykowski, C. J. van der Beek, M. A. Tanatar, H. Luo, and Z. Wang, B. Shen, H.-H. Wen, and R. Prozorov, Phys. Rev. B **86**, 024515 (2012).

[79] R. Griessen, H.-h. Wen, A. J. J. van Dalen, B. Dam, J. Rector, H. G. Schnack, S. Libbrecht, E. Osquiguil, and Y. Bruynseraede, Phys. Rev. Lett. **72**, 1910 (1994).

[80] V. Mishev, M. Nakajima, H. Eisaki, and M. Eisterer, Sci. Rep. **6**, 27783 (2016).

[81] D. K. Pratt, W. Tian, A. Kreyssig, J. L. Zarestky, S. Nandi, N. Ni, S. L. Bud'ko, P. C. Canfield, A. I. Goldman, and R. J. McQueeney, Phys. Rev. Lett. **103**, 087001 (2009).

[82] E. Wiesenmayer, H. Luetkens, G. Pascua, R. Khasanov, A. Amato, H. Potts, B. Banusch, H. H. Klauss, and D. Johrendt, Phys. Rev. Lett. **107**, 237001 (2011).

[83] Z. Li, R. Zhou, Y. Liu, D. L. Sun, J. Yang, C. T. Lin, and G.-q. Zheng, Phys. Rev. B **86**, 180501(R) (2012).

[84] B. Kalisky, J. R. Kirtley, J. G. Analytis, J.-H. Chu, A. Vailionis, I. R. Fisher, and K. A. Moler, Phys. Rev. B **81**, 184513 (2010).

[85] B. Kalisky, J. R. Kirtley, J. G. Analytis, J.-H. Chu, I. R. Fisher, and K. A. Moler, Phys. Rev. B **83**, 064511 (2011).

[86] C. Putzke, P. Walmsley, J. D. Fletcher, L. Malone, D. Vignolles, C. Proust, S. Badoux, P. See, H. E. Beere, D. A. Ritchie, S. Kasahara, Y. Mizukami, Y. Shibauchi, Y. Matsuda, and A. Carrington, Nat. Commun. **5**, 5679 (2014).

[87] M. Fujioka, S. J. Denholme, M. Tanaka, H. Takeya, T. Yamaguchi, and Y. Takano, Appl. Phys. Lett. **105**, 102602 (2014).

[88] P. J. W. Moll, L. Balicas, V. Geshkenbein, G. Blatter, J. Karpinski, N. D. Zhigadlo, and B. Batlogg, Nat. Mater. **12**, 134 (2013).